Research Square

Preprints are preliminary reports that have not undergone peer review.
They should not be considered conclusive, used to inform clinical practice,
or referenced by the media as validated information.

Influence of Crystallographic and Microstructural Features on Magneto-crystalline Anisotropy and Magnetization Reversal in Al-Doped Ni Thin Films

Qurat Ul Ain
University of the Punjab
Ali Tahir
aleetahir32@gmail.com

University of the Punjab
Anam Ayub Tahami
University of the Punjab
Arzoo Fatima
University of the Punjab

Research Article

Keywords: Thin Film, Sputtering, magnetization reversal, Reflectivity, magneto anisotropy

Posted Date: October 26th, 2026

DOI: https://doi.org/10.21203/rs.3.rs-11390201/v1

License: This work is licensed under a Creative Commons Attribution 4.0 International License.
Read Full License

Additional Declarations: No competing interests reported.

Influence of Crystallographic and Microstructural Features on Magneto-crystalline Anisotropy and Magnetization Reversal in Al-Doped Ni Thin Films

Qurat Ul Ain[1], Ali Tahir*[1‡], Anam Ayub Tahami[1], Arzoo Fatima[1],

[1]Centre of Excellence in Solid State Physics, University of the Punjab, Lahore 54590, Pakistan

[‡]Qurat Ul Ain and Ali Tahir contributed equally to this work.

*Corresponding Author: Ali Tahir, Email: aleetahir32@gmail.com

Research Highlights

- Al-doped Ni thin films (0-5 wt.% Al) were grown by co-sputtering on Si/SiO_2 substrates.
- Increasing Al contracts the Ni lattice, refines crystallites, and raises microstrain and dislocation density.
- The 3 wt.% Al film gives the lowest coercivity (80 Oe), highest squareness (0.708), and highest susceptibility (0.0208 Oe^{-1}).
- Excess Al broadens the switching-field distribution, promotes multistep reversal, and decouples coercivity from grain size.

Graphical Abstract

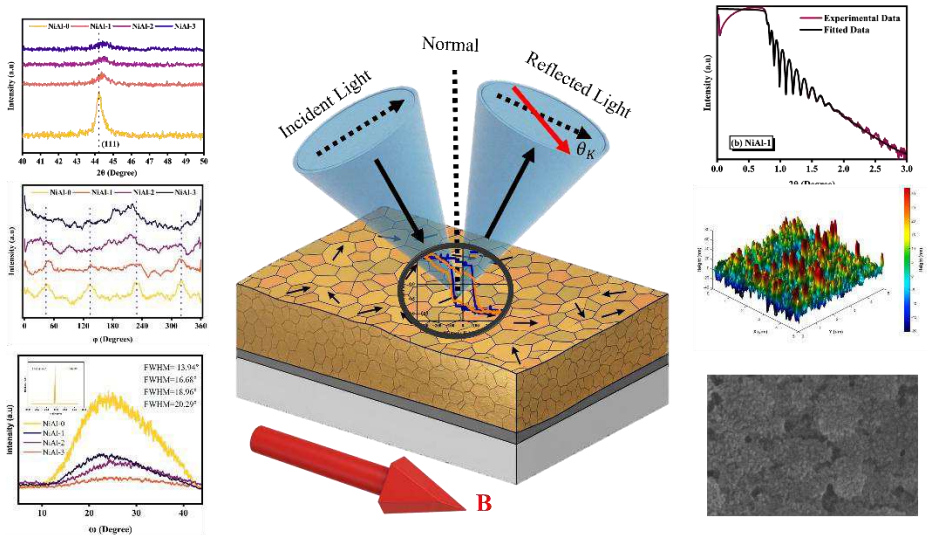

Abstract

The role of controlled doping in tuning magneto-crystalline anisotropy and magnetization reversal in polycrystalline Ni nanocomposite thin films through crystallographic and microstructural modification remains inadequately addressed. This study examines magnetron-sputtered Al-doped Ni thin films containing 0, 2, 3, and 5 wt.% Al deposited on Si/SiO_2 substrates. Al incorporation progressively contracts the Ni lattice and refines the crystallite size while increasing microstrain, dislocation density, and mosaic spread, collectively degrading the crystallographic texture. These structural changes arise from substitutional lattice distortion and solute-limited adatom mobility, which suppress grain growth and promote re-nucleation. XRR and AFM further show that Al reduces film density and produces a non-monotonic surface roughness, with the smoothest and most uniform surface at the intermediate composition. The resulting magnetic behavior is non-monotonic. The undoped film exhibits a preferred 0° direction with a loop displacement of approximately 48 Oe, arising from interfacial exchange coupling with a naturally formed antiferromagnetic NiO layer. At 5 wt.% Al, the balance between reduced pinning and moderate structural disorder produces the most favorable response, with the lowest easy-axis coercivity (80.0 ± 0.5 Oe), highest squareness (0.708 ± 0.003), and highest initial susceptibility (0.0208 ± 0.0005 Oe^{-1}). Beyond this optimum, excessive lattice strain and defect accumulation broaden the distribution of local switching fields, increasing coercivity to 128.0 ± 0.5 Oe and promoting multistep reversal. The results further show that coercivity deviates from classical grain-size scaling and is governed more strongly by mosaic spread and defect density, while surface roughness limits the low-field susceptibility. These findings demonstrate that moderate Al incorporation provides effective control over magnetic anisotropy and reversal, whereas excessive doping destabilizes the reversal pathway through disorder-dominated pinning.

Keywords: Thin Film, Sputtering, magnetization reversal, Reflectivity, magneto anisotropy

Introduction

Magnetic thin films are central to spintronic, magnetic sensing, and data storage technologies because their magnetic properties can be tailored through nanoscale control of composition, crystallographic structure, morphology, and interfaces. In polycrystalline films, these structural characteristics determine the mechanisms of magnetization reversal and consequently govern technologically relevant parameters such as coercivity, remanence, magnetic squareness, and anisotropy [1]. Establishing quantitative relationships between structure and properties is therefore essential for controlling magnetic behavior in thin film systems. Previous studies have

demonstrated that deposition conditions can substantially modify the crystal structure, grain evolution, crystallographic texture, and magnetic response of sputtered magnetic films [2]. Among transition metal thin films, Ni is particularly attractive because of its ferromagnetic character, relatively high Curie temperature of approximately 627 K, and compatibility with thin film device architectures. Ni films have therefore been investigated for magnetic shielding, flux concentration, magnetic electrodes, and spintronic heterostructures. However, their magnetic response is highly sensitive to crystallite size, lattice strain, defect density, surface roughness, and crystallographic texture [3]. These parameters influence magnetization nucleation, rotation, domain wall propagation, and reversal, producing substantial variations in coercivity and magnetic squareness [4].

Hedayati et al. (2014) reported that the magnetic properties of electrodeposited Ni thin films are sensitive to electrode rotation speed, with coercivities remaining below 110 Oe across the investigated deposition conditions [5]. Strain engineering has been demonstrated as an effective approach for tuning magnetic anisotropy in spinel ferrite thin films. In Ni–Zn ferrite films, varying in-plane strain from −0.6% compressive to +0.5% tensile changed the magnetic anisotropy from −14.3 kJ m^{-3} (in-plane) to 0.1 kJ m^{-3} (nearly out-of-plane), accompanied by lattice and Raman changes and strain-dependent hard and soft magnetic phases [6] . For DC-magnetron-sputtered Fe thin films, increasing deposition time promoted grain growth and a transition from island-like to layered growth, while the surface roughness decreased and stabilized at longer deposition times. The films exhibited polycrystalline bcc Fe with preferential (110) orientation, with the 120 s film showing optimal magnetic properties, including Ms = 1567 emu cm^{-3}, Hc = 92 Oe, and Mr/Ms = 0.86 [7].

In polycrystalline ferromagnetic films, crystallographic texture and structural disorder are particularly important because they determine the spatial distribution of local magnetic easy axes [8]. Mosaic spread, defined by the angular distribution of crystallite orientations, can consequently modify the macroscopic magnetic anisotropy and broaden the distribution of switching fields [9]. Lattice strain and defects can further perturb the local magneto-crystalline anisotropy energy and introduce spatial variations in the energy landscape experienced during magnetization reversal. These effects may manifest as changes in coercivity, remanence, switching-field distribution, and reversal mode. Despite the established importance of these structural parameters, their quantitative relationship with magnetic behavior in Ni-based polycrystalline thin films remains insufficiently resolved. In particular, structural characterization and magnetic measurements are frequently discussed independently, limiting

a direct understanding of the influence of composition-induced structural disorder on magnetization reversal [10].

Alloying with a non-magnetic element provides an effective route for systematically modifying the structural state of Ni while minimizing additional magnetic contributions from the alloying species. Aluminum is particularly suitable for this purpose because its atomic radius (0.143 nm) is larger than that of Ni (0.125 nm), allowing its incorporation into the Ni lattice to introduce local lattice distortion and strain. Al incorporation can also influence grain growth through solute drag and grain boundary pinning, potentially promoting grain refinement and modifying the crystallographic texture. Because Al is essentially nonmagnetic in the present context, changes in the magnetic response can primarily be associated with its effects on the Ni crystal structure, defects, texture, morphology, and interfaces rather than the introduction of an additional magnetic sublattice. Its high affinity for oxygen may also modify the chemical state of interfaces and surface regions, providing an additional means of influencing interfacial magnetic behavior. Thus, controlled Al incorporation offers a useful strategy for investigating the relationship between compositional disorder, crystallographic structure, and magnetic reversal in Ni thin films [11], [12].

This work systematically investigates magnetron-sputtered polycrystalline Ni-Al thin films with 0, 2, 3, and 5 wt.% Al to establish correlations between Al-induced structural evolution and magnetic behavior. By integrating complementary structural and magnetic probes, the study quantitatively evaluates the roles of crystallographic texture, mosaic spread, lattice strain, crystallite size, defects, and surface morphology in determining magnetic anisotropy and magnetization reversal. High-resolution X-ray diffraction (HRXRD) is employed to identify the crystallographic phase, and preferred orientation, while rocking-curve (ω-scan) analysis quantifies the out-of-plane mosaic spread and crystallite tilt that govern the angular distribution of local easy axes. Complementary φ-scan measurements probe the in-plane rotational symmetry and texture quality, thereby revealing the degree of in-plane crystallographic alignment. X-ray reflectivity (XRR) provides independent, non-destructive assessment of film thickness, density, interfacial and surface roughness, which are critical for interpreting strain state and growth quality. Field-emission scanning electron microscopy (FESEM) and atomic force microscopy (AFM) resolve the surface and grain morphology, linking nanoscale grain refinement and roughness to grain-boundary density and domain-wall pinning sites, while energy-dispersive X-ray spectroscopy (EDS) confirms the elemental composition and verifies the intended Al incorporation. Finally, magneto-optical Kerr effect (MOKE) magnetometry

directly measures the in-plane magnetic anisotropy and magnetization reversal, providing the coercivity, squareness, initial susceptibility, and loop shape needed to correlate the structural state with the field-driven switching behavior. Together, these complementary techniques establish a complete framework connecting controlled Al incorporation to the structural and magnetic response of Ni thin films. This framework provides a quantitative basis for tailoring Ni-based magnetic layers through compositional engineering for spintronic and magnetic device applications.

Experimental Details

Thin film structures were fabricated using a multi-gun magnetron sputtering system (VTS-DaON 1000). Structural and interfacial properties were investigated using high-resolution X-ray diffraction (HRXRD), and X-ray reflectivity (XRR) (Rigaku SmartLab SE). Surface morphology and topography were analyzed using atomic force microscopy (AFM) (Park Systems XE7). Energy-dispersive X-ray spectroscopy (EDX) using an Oxford external detector connected to a Nano Nova FESEM was used to evaluate the elemental composition.. Magnetic properties were characterized using a laboratory-built magneto-optical Kerr effect (MOKE) setup.

Fabrication of thin films

The pure and Al-doped Ni thin films were deposited on commercially available single-crystal Si (100) substrates coated with a 300 nm thermally grown SiO_2 layer using a multi-gun magnetron sputtering system. Prior to deposition, the substrates were sequentially ultrasonically cleaned in ethanol, isopropyl alcohol (IPA), and deionized (DI) water for 5 min each to remove organic and particulate contaminants. The target-to-substrate distance was fixed at 7 cm for all depositions. High-purity Ni (99.95%) and Al (99.99%) targets were used as source materials. The sputtering chamber was evacuated to a base pressure of 2.5×10^{-7} Torr to minimize residual gas contamination. High-purity argon (99.99%) was introduced as the sputtering gas, and the working pressure was maintained at 5×10^{-3} Torr during deposition. Ni thin films were deposited using DC magnetron sputtering at a constant power of 120 W. Al doping was achieved via co-sputtering from a separate DC-powered Al target, with applied powers of 5.8 W, 8.7 W, and 11.6 W to obtain approximately 2, 3, and 5 wt.% Al concentrations, respectively. The samples were named as NiAl-0, 1,2 and 3 respectively.

(a) (b)

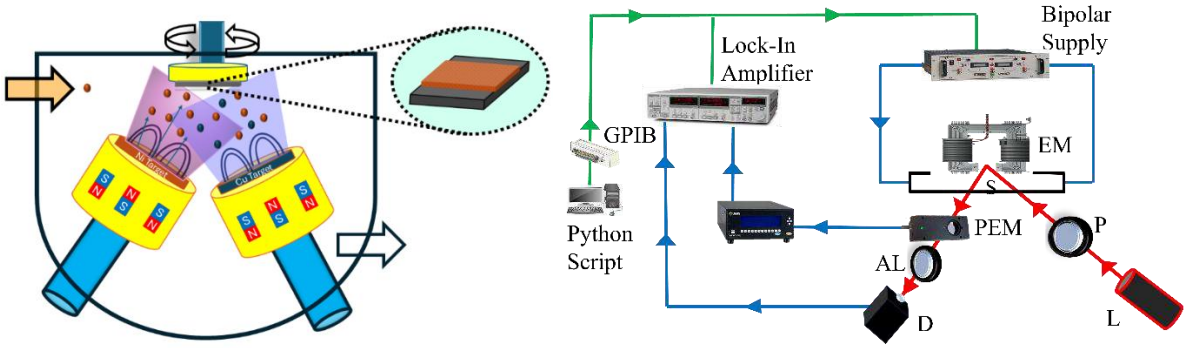

Figure 1: (a) Schematic of magnetron sputtering multi-gun unit used for the fabrication of the thin films (b) and MOKE measurement setup. a laser beam passes through a polarizer (P) and is directed by lenses (L) onto the sample (S), positioned inside an electromagnet (EM). The reflected beam then passes through an analyzer (A) before reaching the detector (D). Electronic instruments (current source, lock-in amplifier, and data acquisition system) control the magnetic field and record the Kerr rotation signal.

The deposition time was optimized to achieve a nominal film thickness of 50 nm for all samples. During deposition, continuous substrate rotation was employed to ensure uniform thickness and compositional homogeneity across the film surface. All depositions were carried out at a substrate temperature of 200 °C. After deposition, the samples were allowed to cool to room temperature under a vacuum of 4.5×10^{-6} Torr. The chamber was then backfilled with high-purity nitrogen (99.99%) before sample retrieval to minimize oxidation and reduce stress-induced defects.

Table 1. Deposition parameters used for the fabrication of the NiAl-s thin films by multi-gun magnetron sputtering.

Parameter	Value
Base pressure	2.5×10^{-7} Torr
Working pressure	5×10^{-3} Torr
Target-to-substrate distance	7 cm
Ni DC Power	120 W
Al DC Power	5.8 W, 8.7 W and 11.6 W

Deposition temperature	200 °C

Magneto Optic Kerr Effect (MOKE) Setup

The magneto-optical Kerr effect (MOKE) system employed in this study was developed in-house to investigate the anisotropy of thin magnetic films. MOKE is based on the rotation and ellipticity changes of linearly polarized light upon reflection from a magnetized surface due to spin–orbit coupling effects, described by the complex Kerr angle:

$$\tilde{\theta}_K = \theta_K + i\epsilon_K$$

Longitudinal MOKE geometry was employed, with the magnetic field applied in-plane and parallel to the plane of incidence, enabling direct evaluation of in-plane magnetization reversal and coercivity changes. A continuous-wave diode laser (λ = 632.8 nm) was used as the light source, delivering coherent illumination that was linearly polarized by a Glan–Thompson polarizer. The beam was subsequently modulated by a photo-elastic modulator (PEM) operating at 50 kHz, which introduced a sinusoidal phase retardation between orthogonal polarization components, thereby enabling phase-sensitive detection of Kerr rotation. The modulated beam was directed onto the magnetic specimen positioned within the gap of a bipolar electromagnet, allowing the application of in-plane magnetic field. The reflected beam passed through an analyzer oriented close to extinction relative to the polarizer and was collected by a fast silicon photodiode detector. The detector output was processed by a lock-in amplifier (Stanford SR830), referenced to the PEM modulation frequency, which isolated the Kerr signal from background noise. The lock-in amplifier was interfaced with a Python-controlled script via GPIB, enabling automated data acquisition, real-time signal processing, and reconstruction of magnetization reversal loops. A bipolar power supply provided precise control of external magnetic fields up to ±1 kOe. The schematic diagram illustrates the integration of optical and electronic components, this configuration provides a versatile platform for magneto-optical characterization, with high signal-to-noise detection [13], [14].

Crystallographic Analysis

Figure 2 shows the X-ray diffraction (XRD) patterns of pure Ni and Al-doped Ni thin films (NiAl-0, NiAl-1, NiAl-2, and NiAl-3). All samples exhibit a prominent diffraction peak located in the range of 2θ = 44.24°–44.68°, which corresponds to the (111) crystallographic plane of face-centered cubic (FCC) Ni, confirming the formation of crystalline metallic Ni. The

enlarged view of the diffraction peaks (Fig 2 (b)) further reveals a gradual shift of the (111) reflection toward higher diffraction angles with increasing Al incorporation. No additional diffraction peaks associated with secondary phases such as NiAl intermetallic compounds or Al-rich oxide phases are detected within the XRD detection limit, indicating that Al atoms are successfully incorporated into the Ni lattice without altering the parent FCC crystal structure [15].

The observed peak shift from 44.24° for NiAl-0 to 44.68° for NiAl-3 indicates a progressive contraction of the Ni lattice. This behavior can be attributed to the substitution of Ni atoms by Al atoms within the crystal lattice, resulting in changes in interatomic spacing and lattice distortion. According to Bragg's law, an increase in diffraction angle corresponds to a decrease in interplanar spacing (d-spacing). Consequently, the calculated d-spacing decreases from 0.20457 nm for NiAl-0 to 0.20266 nm for NiAl-3, confirming the gradual lattice contraction induced by Al incorporation [16].

The broadening of the diffraction peak becomes more pronounced with increasing Al content, as reflected by the increase in full width at half maximum (FWHM) from 0.425° for NiAl-0 to 0.986° for NiAl-3. Peak broadening is generally associated with reduced crystallite size and increased lattice imperfections. Using the Scherrer equation, the crystallite size was estimated to be 20.18 nm for the undoped Ni film, which decreases significantly to 11.81 nm, 12.14 nm, and 8.71 nm for NiAl-1, NiAl-2, and NiAl-3, respectively. This reduction demonstrates that Al addition suppresses grain growth and promotes grain refinement during film formation [17].

The decrease in crystallite size is accompanied by a considerable increase in lattice strain and dislocation density. The microstrain increases from 0.00456 in NiAl-0 to 0.01047 in NiAl-3, while the dislocation density rises from 2.46×10^{-3} nm^{-2} to 1.32×10^{-2} nm^{-2}. The increase in these parameters suggests that Al incorporation introduces lattice distortions and internal stresses, leading to the generation of additional crystallographic defects and grain boundaries. Such behavior is commonly observed in substitutionally doped metallic thin films, where the presence of dopant atoms hinders crystal growth and enhances defect formation [18].

The lattice parameter (a) also exhibits a systematic reduction with increasing Al concentration, decreasing from 0.35432 nm for NiAl-0 to 0.35101 nm for NiAl-3. A similar trend is observed for the unit-cell volume, which decreases from 0.04448 nm^3 to 0.04325 nm^3. The reduction in lattice parameter and unit-cell volume further supports the successful incorporation of Al atoms into the Ni matrix and confirms the contraction of the FCC lattice. The continuous decrease in

these structural parameters without the appearance of secondary phases suggests the formation of a solid-solution-type Ni-Al alloy structure [19].

Table 2. XRD-derived structural parameters (2θ, FWHM, crystallite size, d-spacing, dislocation density, microstrain, and lattice parameter) for NiAl-0 to NiAl-3.

2θ	FWHM	Crystallite Size(nm)	d-spacing(nm)	Dislocation Density (nm^{-2})	Strain	a(nm)
44.24	0.425	20.17	0.2045	0.00245	0.0045	0.3543
44.50	0.727	11.80	0.2034	0.00717	0.0077	0.3523
44.56	0.707	12.14	0.2031	0.00678	0.0075	0.3519
44.68	0.986	8.71	0.2026	0.0131	0.0104	0.3510

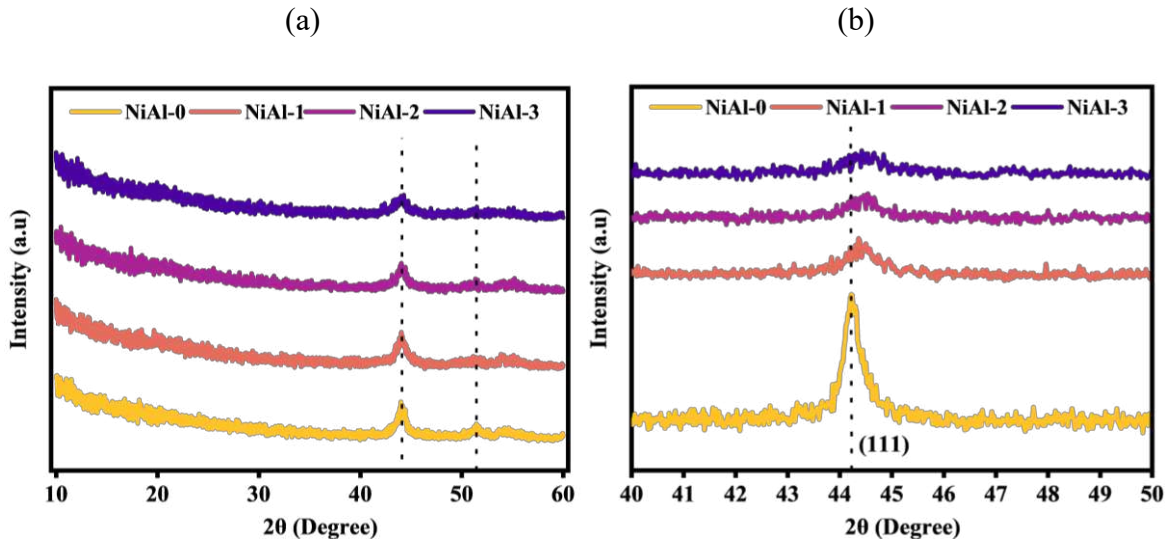

Figure 2. XRD patterns of the pure and Al-doped Ni thin films (NiAl-0 to NiAl-3): (a) wide-range 2θ scans from 10° to 60° and (b) enlarged view of the (111) reflection between 40° and 50°.

The ω-scan (rocking curve) probes the distribution of crystallographic plane orientations about the surface normal and is a direct measure of out-of-plane mosaic spread (crystal tilt). The NiAl films exhibit broad rocking-curve peaks with FWHM values increasing from 13.94° (NiAl-0)

to 16.68° (NiAl-1), 18.96° (NiAl-2), and 20.29° (NiAl-3), indicating a progressive increase in mosaicity and crystallite misorientation with Al incorporation. The broadening is attributed to Al-induced lattice distortion, strain accumulation, and defect formation, which promote grain tilting and degrade the out-of-plane texture. In contrast, the inset Si (400) rocking curve of the Si (100) substrate exhibits an extremely narrow FWHM of 0.1°, confirming both the high crystalline quality of the single-crystal substrate and the reliability of the measurement technique. Therefore, the large FWHM values observed for the NiAl films are intrinsic to the sputtered thin films and reflect their high mosaic spread rather than any instrumental broadening or substrate-related effects [20].

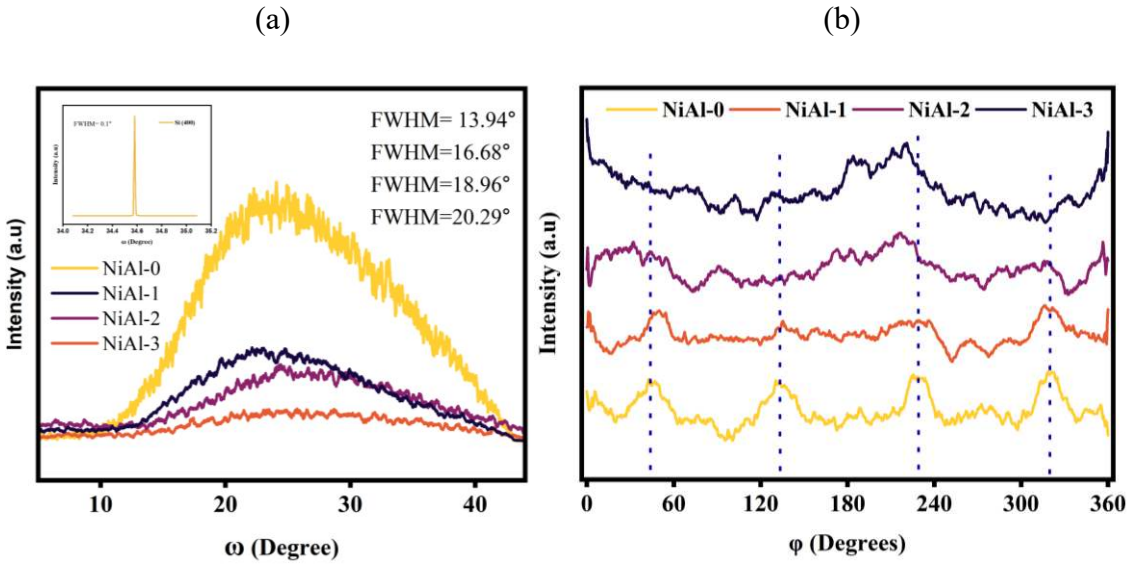

Figure 3. (a) ω-scan (rocking curve) profiles of NiAl-0 to NiAl-3, showing the out-of-plane mosaic spread. The inset shows the Si (400) rocking curve of the substrate (FWHM ≈ 0.1°). (b) φ-scan profiles of the same films, showing the in-plane rotational symmetry and its progressive degradation with Al incorporation.

The φ-scan (in-plane XRD) measures the rotational symmetry and in-plane crystallographic orientation of a selected set of lattice planes by rotating the sample about its surface normal while maintaining the diffraction condition. The undoped Ni film (NiAl-0) exhibits four distinct peaks separated by approximately 90°, indicating a well-defined fourfold in-plane rotational symmetry and the presence of a preferred in-plane texture. The equal angular spacing confirms the existence of crystallographic domains aligned along equivalent orientations, reflecting a relatively ordered in-plane arrangement of grains.

With Al incorporation, the φ-scan peaks gradually broaden, weaken, and shift from their original angular positions. The peak shifts suggest a modification of the in-plane lattice orientation caused by Al-induced lattice distortion and residual strain, while the reduction in peak intensity indicates a deterioration of in-plane texture and a decrease in the fraction of coherently aligned crystallites. At higher Al concentrations, the peaks become less distinct and more diffuse, evidencing increased orientational disorder and a wider distribution of in-plane grain orientations. These results demonstrate that Al doping progressively disrupts the in-plane crystallographic ordering of the Ni films, leading to enhanced mosaicity and reduced texture quality [21], [22].

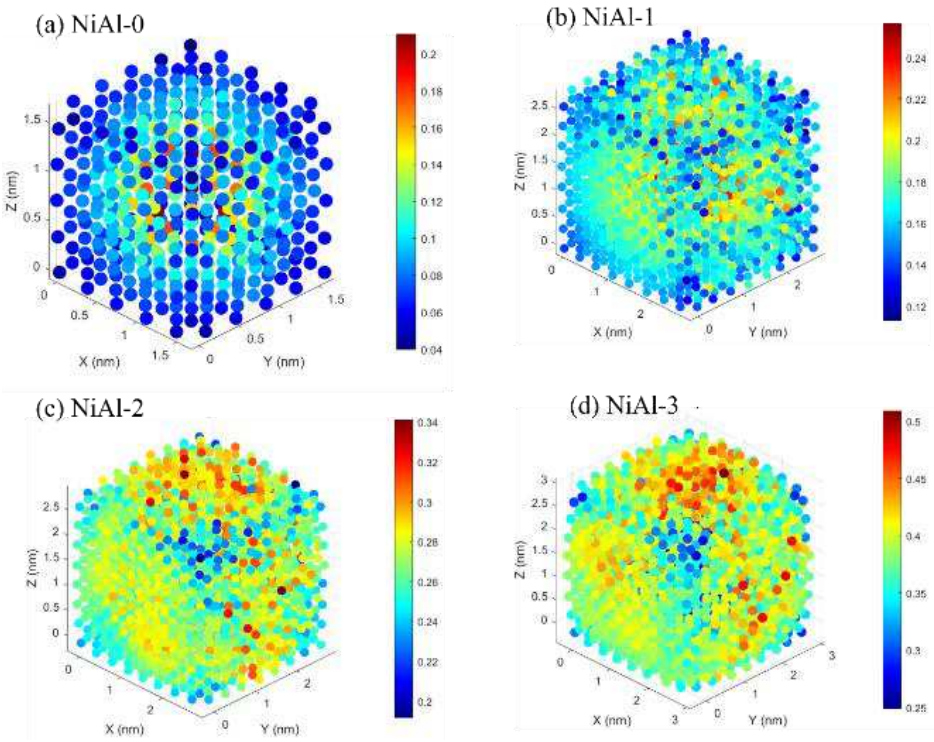

Figure 4. Numerically reconstructed defect and crystallographic disorder maps of the Al-doped Ni thin films (NiAl-0 to NiAl-3): atomic displacement fields reconstructed from the experimentally determined lattice strain and dislocation density/

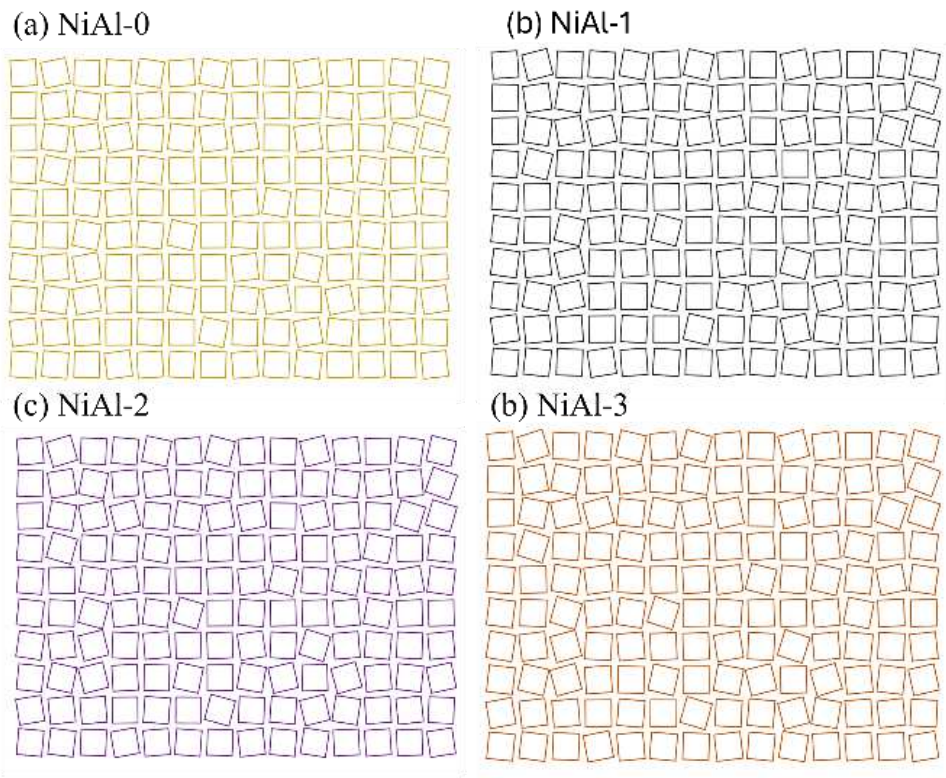

Figure 5 Crystallite orientation maps reconstructed from the experimentally determined mosaic spread, showing the progressive increase in crystallite misorientation and degradation of out-of-plane texture.

To further elucidate the influence of Al incorporation on the defect state, atomic displacement fields were numerically reconstructed in MATLAB using the experimentally determined lattice strain and dislocation density derived from XRD analysis, as shown in Fig. 4. The simulations reveal a progressive increase in both the magnitude and spatial heterogeneity of atomic displacements with increasing Al content, indicating enhanced local lattice distortion associated with defect accumulation. The evolution of the displacement field is consistent with the increase in microstrain and dislocation density, providing a three-dimensional visualization of the defect landscape and further confirming that Al incorporation progressively perturbs the Ni crystal lattice. This defect evolution is expected to play a key role in governing the subsequent changes in crystallographic texture and magnetic anisotropy. To provide a direct visualization of the crystallographic disorder, the experimentally determined mosaic spread was reconstructed as a crystallite orientation map, as shown in Fig. 5. The progressive increase in crystallite misorientation with Al incorporation reflects the broadening of the rocking curve and confirms the gradual degradation of out-of-plane texture. The larger angular dispersion of

crystallite orientations indicates reduced epitaxial coherence and enhanced mosaicity arising from Al-induced lattice distortion and defect accumulation. These results are consistent with the increase in microstrain and dislocation density obtained from XRD, demonstrating that Al incorporation progressively disrupts the crystallographic alignment of the Ni thin films [23], [24].

X-Ray Reflectivity

X-ray reflectivity measurements were employed to investigate the structural quality of the magnetron-sputtered NiAl thin films. The reflectivity profiles exhibit a well-defined critical angle (θc = 0.7–0.8°) followed by pronounced Kiessig oscillations originating from the interference of X-rays reflected from the film surface and the film/substrate interface. The oscillation periodicity is governed by the film thickness according to $\Delta q = 2\pi/t$, where $q = (4\pi\sin\theta)/\lambda$ is the scattering vector and t is the film thickness. The excellent agreement between the experimental and fitted curves confirms the reliability of the reflectivity model [25].

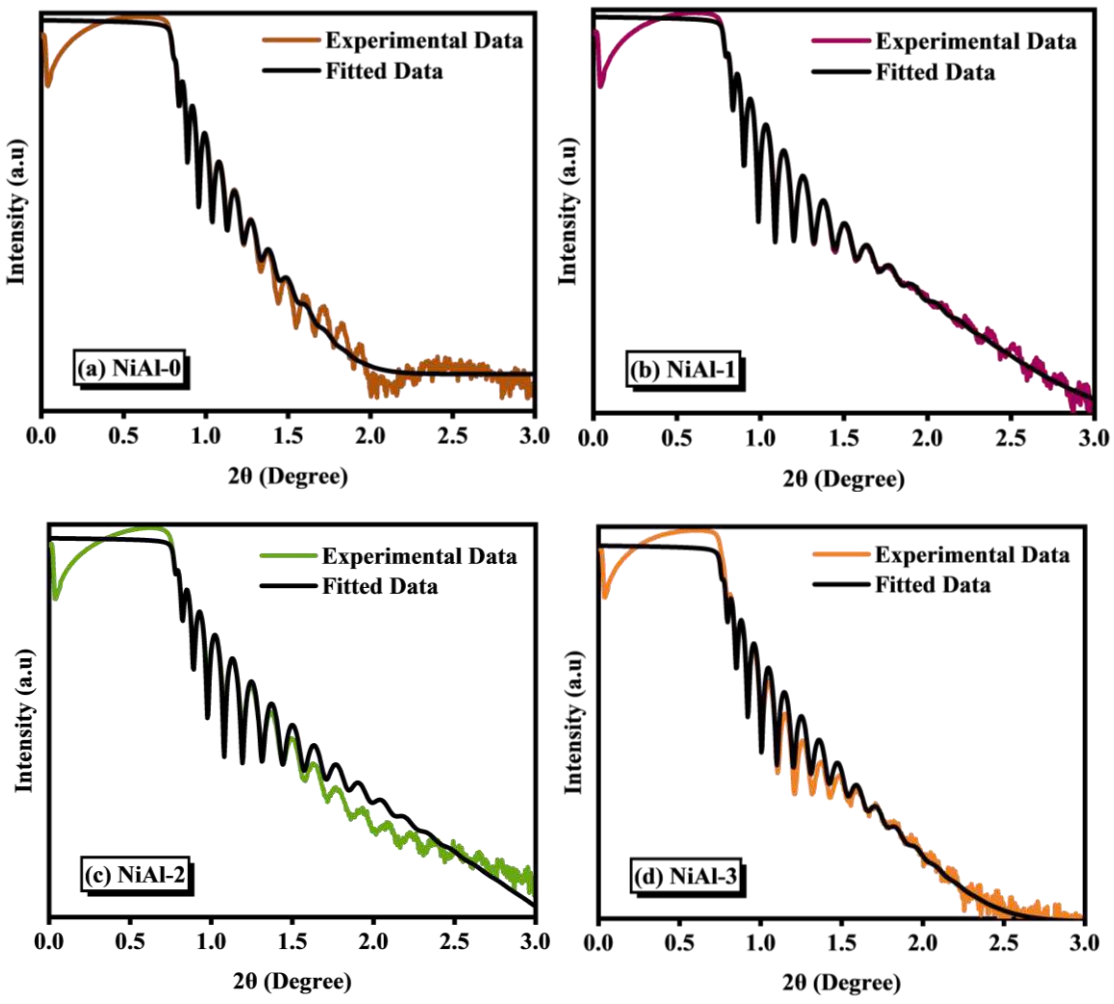

Figure 6. X-ray reflectivity profiles of the Al-doped Ni thin films: (a) NiAl-0, (b) NiAl-1, (c) NiAl-2, and (d) NiAl-3. Experimental data are shown together with the corresponding fitted curves.

The undoped NiAl-0 film exhibits distinct Kiessig fringes up to 2.0°, with a fitted thickness of 55.755 ± 0.15 nm, density of 8.75384 ± 0.04 g cm^{-3}, and surface roughness of 2.975 ± 0.03 nm. Upon Al incorporation, NiAl-1 shows the most persistent oscillations extending up to 3°, accompanied by the slowest reflectivity decay. This behavior is associated with its increased thickness of 57.984 ± 0.05 nm, while the reduced density of 8.31894 ± 0.013 g cm^{-3} reflects the incorporation of lower-density Al into the Ni matrix. NiAl-2 also exhibits well-resolved fringes over a broad angular range, with a thickness of 57.777 ± 0.19 nm, density of 8.10679 ± 0.04 g cm^{-3}, and roughness of 1.992 ± 0.03 nm. The lower density compared with NiAl-0 is consistent with the progressive substitution of Ni by Al within the film. In contrast, NiAl-3 displays a more pronounced attenuation of the oscillatory pattern beyond 2.3-2.5°, with a thickness of 55.612 ± 0.3 nm, density of 7.78167 ± 0.05 g cm^{-3}, and roughness of 2.432 ± 0.1 nm. The stronger damping of the Kiessig fringes is attributed to the increased surface roughness, which enhances diffuse scattering and reduces fringe visibility at higher scattering angles [26], [27].

The quality of the fits is confirmed by the R-factors, which remain low for all samples: 3.739% (NiAl-0), 2.144% (NiAl-1), 5.042% (NiAl-2), and 4.381% (NiAl-3). The lowest R-factor obtained for NiAl-1 indicates the most reliable fit, consistent with its persistent and well-defined oscillations, whereas the slightly higher values for NiAl-2 and NiAl-3 reflect the increased interfacial and surface disorder in these films. The substrate roughness extracted from the fits decreases from 1.820 ± 0.017 nm for NiAl-0 to 0.954 ± 0.007 nm for NiAl-1 and 0.906 ± 0.013 nm for NiAl-2, before increasing to 1.330 ± 0.02 nm for NiAl-3, indicating that the initial stages of Al incorporation produce a smoother film/substrate interface, while higher Al content reintroduces interfacial disorder [28].

These results demonstrate that Al incorporation systematically influences the growth kinetics and microstructural evolution of sputtered Ni films, affecting film densification, interface quality, and surface morphology. The monotonic decrease in film density from 8.75 to 7.78 g cm^{-3} with increasing Al content is consistent with the substitution of higher-density Ni by lower-density Al, while the non-monotonic roughness trend reflects the competing effects of Al-modified adatom mobility and defect accumulation during growth [29].

Table 3. XRR fitting parameters for NiAl-0, NiAl-1, NiAl-2, and NiAl-3, including film thickness, film density, film roughness, and substrate roughness. The Si substrate density was fixed at 2.32924 g/cm³, and its thickness was treated as infinite.

Sample	Film thickness (nm)	Film density (g/cm³)	Film roughness (nm)	Substrate roughness (nm)
NiAl-0	55.755 ± 0.15	8.75384 ± 0.04	2.975 ± 0.03	1.820 ± 0.017
NiAl-1	57.984 ± 0.05	8.31894 ± 0.013	2.192 ± 0.011	0.954 ± 0.007
NiAl-2	57.777 ± 0.19	8.10679 ± 0.04	1.992 ± 0.03	0.906 ± 0.013
NiAl-3	55.612 ± 0.3	7.78167 ± 0.05	2.432 ± 0.1	1.330 ± 0.02

Atomic Force Microscopy Analysis

The surface topography of the pure and Al-doped Ni thin films was examined by atomic force microscopy over a 5 × 5 μm² scan area. Figure 7 shows the three-dimensional AFM topography images of NiAl-0, NiAl-1, NiAl-2, and NiAl-3, and the extracted surface parameters, including grain size, average roughness (Ra), root-mean-square roughness (Rq), and peak-to-valley height (Rt), are listed in Table 4.

The NiAl-0 film exhibits a granular surface with an average grain size of 296.29 nm and roughness values of Ra = 8.3687 nm, Rq = 10.9626 nm, and Rt = 87.5538 nm. In the absence of Al, Ni adatoms retain sufficient surface mobility during deposition to diffuse across the substrate, leading to nucleation and subsequent grain coarsening through coalescence. This growth pathway produces a relatively ordered granular surface with moderate roughness, consistent with the limited lattice distortion and larger crystallite size indicated by the diffraction data [30].

The NiAl-1 film shows a pronounced increase in grain size and roughness, with the average grain size rising to 362.66 nm and Ra, Rq, and Rt increasing to 17.0769, 23.6209, and 250.0716 nm, respectively. The 3D image reveals the highest vertical relief among all samples. The introduction of Al modifies the growth kinetics by reducing Ni adatom mobility and introducing solute species at the growth front. This can delay coalescence and promote uneven island growth, resulting in a coarser and more topographically heterogeneous surface. The increased structural disorder inferred from the diffraction and rocking-curve data is consistent with this disrupted growth pathway [31].

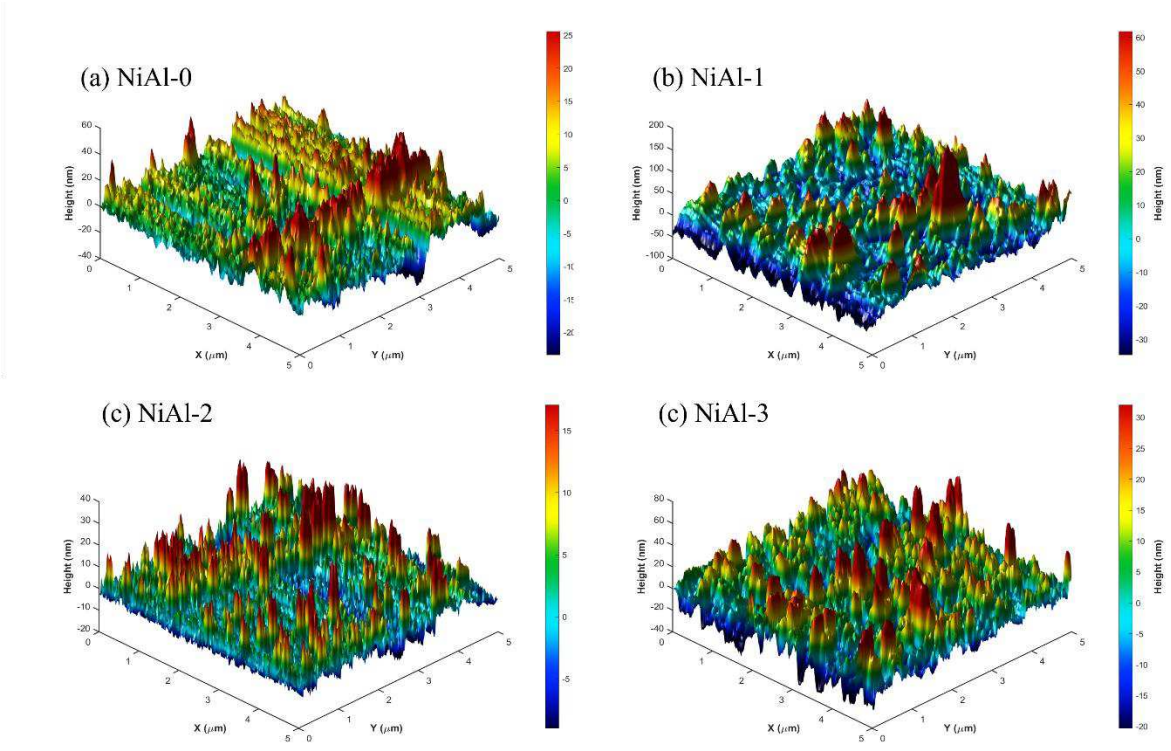

Figure 7. 3D AFM topography images (5 × 5 μm²) of NiAl-0, NiAl-1, NiAl-2, and NiAl-3.

The NiAl-2 film exhibits the smoothest surface in the series, with the average grain size decreasing to 276.06 nm and the roughness parameters reaching their lowest values (Ra = 4.0525 nm, Rq = 5.7017 nm, and Rt = 50.7965 nm). At this intermediate Al content, the growth process appears to reach a favorable balance in which Al incorporation promotes continuous re-nucleation and denser packing while avoiding excessive disruption of adatom diffusion. The resulting film displays a more uniform granular arrangement and reduced height variation, consistent with the improved film density and intermediate structural parameters obtained from the complementary measurements [32].

Table 4. AFM-derived surface parameters of NiAl-0 to NiAl-3, including average grain size, Ra, Rq, and Rt.

Sample Name	Grain Size (nm)	R_a (nm)	R_q (nm)	R_t (nm)
NiAl-0	296.29	8.3687	10.9626	87.5538
NiAl-1	362.66	17.0769	23.6209	250.0716
NiAl-2	276.06	4.0525	5.7017	50.7965
NiAl-3	265.96	9.9996	12.7390	95.8783

The NiAl-3 film shows a renewed increase in roughness, with Ra, Rq, and Rt rising to 9.9996, 12.7390, and 95.8783 nm, respectively, while the average grain size decreases to 265.96 nm. At the highest Al concentration, the growth front is increasingly perturbed by solute accumulation, restricted adatom mobility, and frequent re-nucleation events, which suppress grain coarsening and promote a finer but less uniform surface. The higher density of grain boundaries and localized growth irregularities is consistent with the enhanced microstrain and mosaic spread observed in this film.

The grain-size distributions extracted from the AFM images, shown in Figure 8, provide further insight into the morphological evolution. NiAl-0 and NiAl-1 both exhibit broad distributions with extended large-grain tails, reaching approximately 800 nm and 1000 nm, respectively, confirming that these films contain the largest grains in the series. The wider distribution and larger grain population in these two samples are attributed to the growth regime in which adatom mobility remains sufficient to sustain coalescence and continuous grain coarsening, so that a fraction of grains grows well beyond the average size. In contrast, NiAl-2 displays a narrow distribution centered near 200-300 nm with a sharply reduced large-grain tail, indicating a more uniform grain population and a growth regime dominated by continuous re-nucleation rather than coarsening. NiAl-3 shows an intermediate distribution with a moderate tail extending to about 700 nm, consistent with partial grain refinement at the highest Al content, where restricted adatom mobility and frequent re-nucleation limit but do not fully suppress the growth of larger grains [33].

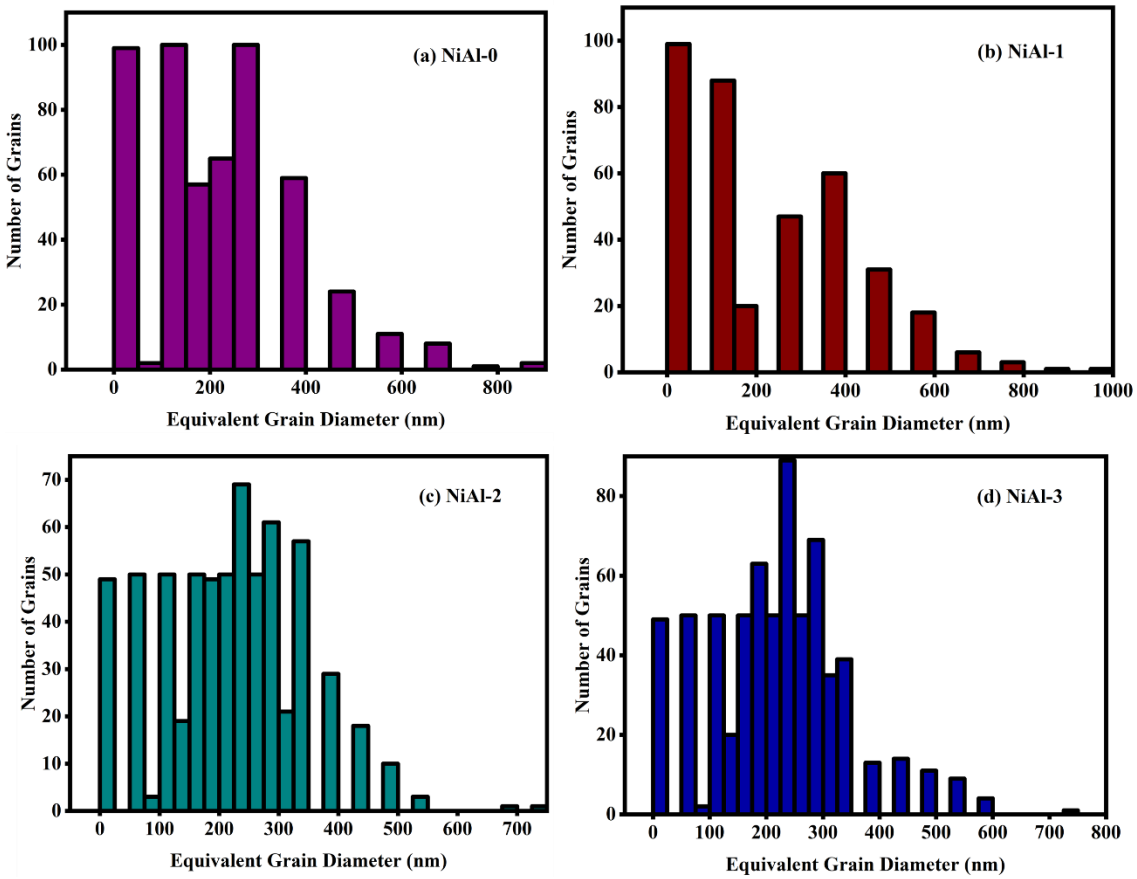

Figure 8. Grain-size distributions extracted from the AFM topography images of the Al-doped Ni thin films: (a) NiAl-0, (b) NiAl-1, (c) NiAl-2, and (d) NiAl-3.

EDS Analysis

The elemental composition of the pure and Al-doped Ni thin films was investigated by energy-dispersive X-ray spectroscopy. Figure 9(a) shows the EDS spectra of NiAl-0, NiAl-1, NiAl-2, and NiAl-3, Figure 9(c–g) presents the elemental maps of the NiAl-3 film, and the corresponding quantitative compositions are summarized in Table 5. All spectra exhibit well-defined peaks corresponding to Ni, Al Si, O, C, and Au. The Ni signal originates from the magnetic layer, whereas the strong Si and O signals arise from the Si/SiO_2 substrate, consistent with the film thickness being smaller than the EDS interaction volume. The C signal is attributed to surface contamination and residual carbon species, and the Au signal originates from the conductive coating applied prior to analysis. An Al Kα peak emerges in the doped films and increases progressively from NiAl-1 to NiAl-3, providing direct confirmation of successful Al incorporation. No peaks corresponding to secondary phases or impurity elements are detected, indicating that the films remain chemically clean within the EDS detection limit [34].

The elemental maps of NiAl-3 (Figure 9(c–g)) reveal a uniform spatial distribution of Ni, Al, Si, O, and C across the analyzed region, with no evidence of clustering, segregation, or localized Al-rich regions. The homogeneous Al map confirms that Al is incorporated uniformly into the Ni matrix rather than forming isolated precipitates, consistent with the solid-solution-type Ni–Al alloy inferred from the diffraction analysis. The overlapping Ni and Al signals further support the co-deposition of both elements within the same layer [35].

The compositions in Table 5, reported in both weight and atomic percentages, show a systematic increase in Al content with increasing Al target power, confirming the intended doping trend, while the Ni content remains comparable across all samples, indicating that Al incorporation does not significantly alter the Ni deposition rate. The C content varies with surface contamination rather than intentional doping, and the low Au content confirms that the conductive coating contributes negligibly to the measured composition. Because the film thickness is considerably smaller than the EDS interaction volume, the measured compositions are dominated by the Si/SiO_2 substrate, as reflected by the high Si and O contents; the Ni and Al values therefore represent relative rather than absolute film stoichiometry [36].

These results confirm the successful and homogeneous incorporation of Al into the Ni matrix, with Al content increasing monotonically with the applied Al target power and no detectable secondary phases, segregation, or impurity elements. The quantitative compositions are consistent with the intended doping trend, although the absolute values are influenced by the substrate contribution and should be interpreted as relative concentrations [37].

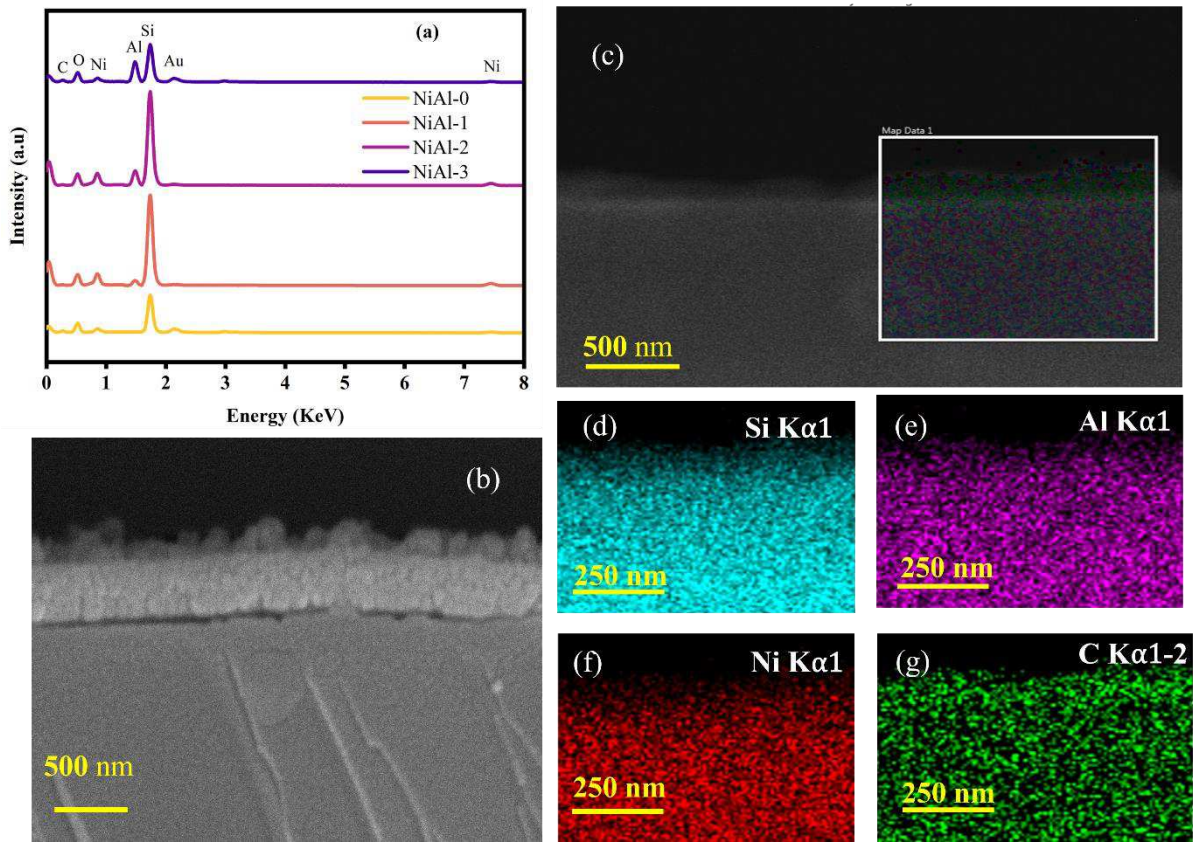

Figure 9. EDS analysis of the Al-doped Ni thin films: (a) EDS spectra of NiAl-0 to NiAl-3, confirming progressive Al incorporation; (b) cross-sectional FESEM image of NiAl-3; (c) cross-sectional image with elemental map overlay; and (d–g) elemental maps of Si, Al, Ni, and C

Table 5. Elemental composition of the Al-doped Ni thin films (NiAl-0 to NiAl-3) obtained from EDS analysis, reported in both weight (wt.%) and atomic (at.%) percentages.

Element	NiAl-0		NiAl-1		NiAl-2		NiAl-4	
	(wt%)	(at.%)	(wt%)	(at.%)	(wt%)	(at.%)	(wt%)	(at.%)
C	4.89	10.10	9.83	18.98	12.39	23.69	5.27	10.66
O	22.49	34.87	22.63	32.80	20.52	29.45	22.38	34.00
Si	54.37	48.02	49.53	40.89	46.36	37.91	51.73	44.77
Ni	15.88	6.71	13.62	5.37	16.20	6.33	14.18	5.87
Al	—	—	1.94	1.67	2.84	2.42	5.02	4.52
Au	2.37	0.30	2.45	0.29	1.69	0.20	1.42	0.18

Total	100.00	100.00	100.00	100.00	100.00	100.00	100.00	100.00

Surface Morphology Analysis

Figure 10 presents the FESEM micrographs of the pure and Al-doped Ni thin films. All films exhibit continuous and compact nanogranular morphologies without evidence of microcracking or film delamination, confirming that Al incorporation does not disrupt the integrity of the sputter-deposited films. The undoped Ni film (NiAl-0) consists of relatively coarse surface grains with well-defined grain boundaries, whereas progressive Al incorporation results in a systematic refinement of the surface morphology, producing increasingly dense assemblies of finer nanograins. The NiAl-3 film exhibits the highest grain packing density and the most homogeneous nanogranular surface among all compositions.

The morphological evolution reflects the influence of Al on thin-film nucleation and growth kinetics during magnetron sputtering. The incorporation of Al modifies surface diffusion and reduces the mobility of deposited Ni adatoms, thereby suppressing competitive grain growth while promoting continuous re-nucleation. Consequently, grain coarsening is inhibited, leading to a finer microstructure with a higher grain-boundary density as the Al concentration increases. Such behavior is characteristic of substitutionally alloyed metallic thin films, where solute atoms impede grain-boundary migration and limit crystallite growth [38].

The FESEM observations are in excellent agreement with the structural parameters extracted from XRD. The progressive reduction in crystallite size from 20.17 nm for NiAl-0 to 8.71 nm for NiAl-3, together with the simultaneous increase in lattice strain and dislocation density, indicates that Al incorporation progressively destabilizes long-range crystalline ordering while increasing the density of lattice imperfections. The refined surface morphology therefore represents the direct microstructural manifestation of the defect-assisted grain-growth suppression identified from the diffraction analysis [39].

From a magnetic perspective, the increase in grain-boundary density is expected to generate a larger population of microstructural pinning sites capable of impeding domain-wall propagation. Simultaneously, the enhanced defect density and local lattice distortion introduce spatial fluctuations in magneto-crystalline anisotropy, producing a broader distribution of switching fields throughout the film. These microstructural modifications are consistent with the evolution of coercivity, squareness ratio, and magnetization reversal behavior observed in the MOKE measurements, establishing a direct correlation between Al-induced defect engineering, crystallographic evolution, and magnetic anisotropy [40].

The cross-sectional FESEM image (Figure 9(b)) shows a continuous and well-adhered film with a uniform thickness of approximately 60 nm, consistent with the XRR-determined values. The film exhibits a slightly granular surface relief at the top, reflecting the island-like nucleation and coalescence characteristic of sputtered metallic films on amorphous substrates. This surface morphology is consistent with the top-view FESEM and AFM observations, which reveal a nanogranular surface with measurable roughness. The film/substrate interface appears sharp and continuous, with no visible voids, cracks, or delamination [40].

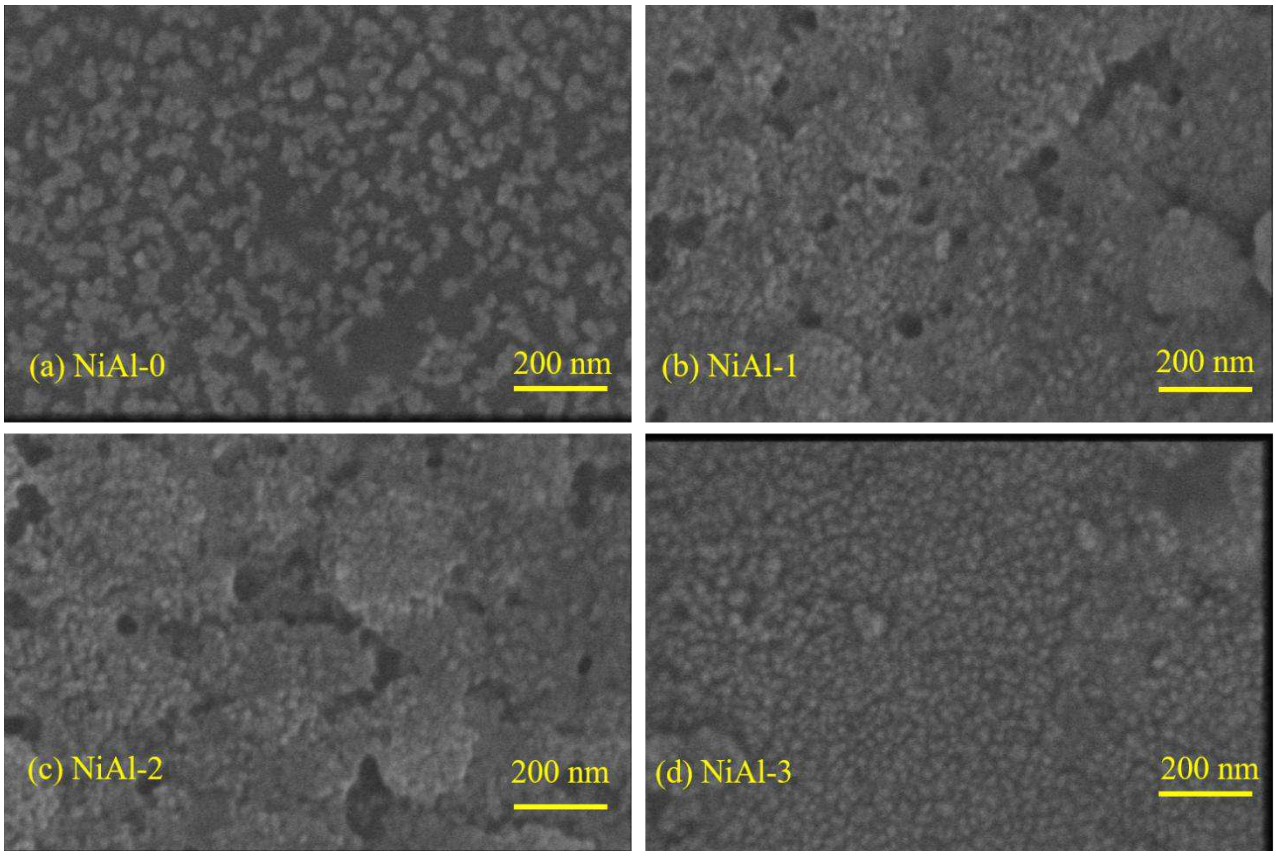

Figure 10. Top-view FESEM micrographs of the Al-doped Ni thin films: (a) NiAl-0, (b) NiAl-1, (c) NiAl-2, and (d) NiAl-3.

Magnetic Anisotropy and Magnetization Reversal Behavior

Longitudinal magneto-optical Kerr effect (MOKE) hysteresis loops were measured with the magnetic field applied along two orthogonal in-plane directions (0° and 90°), as shown in Fig. 11(a–d). The corresponding parameters extracted from the Kerr-field loops are summarized in Table 6. In the longitudinal configuration, the Kerr signal is proportional to the in-plane magnetization component parallel to the applied field; thus, the angular dependence of the loop shape directly reflects the preferred magnetization direction. The average coercivity ($\langle Hc \rangle$), squareness (S = Mr/Ms), initial susceptibility (χ_0), and loop area characterize distinct aspects of the field-driven reversal [41].

The undoped NiAl-0 film exhibits its preferred Kerr response along 0°, with ⟨Hc⟩ = 116.2 ± 0.5 Oe and S = 0.545 ± 0.003, compared with 109.0 ± 0.5 Oe and 0.521 ± 0.003 at 90°. An exchange bias of 48 Oe is observed along the easy axis. This shift arises from interfacial exchange coupling between the ferromagnetic Ni and a naturally formed antiferromagnetic NiO layer at the film surface or interface. The unidirectional anisotropy established by pinned AFM spins at the FM/AFM interface produces the observed loop displacement along the easy axis. The modest difference in Hc and S between the two directions indicates comparable switching characteristics, with a slight preference for 0°. The initial susceptibility increases from 0.00464 ± 0.00005 Oe^{-1} at 0° to 0.01238 ± 0.00005 Oe^{-1} at 90°, indicating that the magnetization component responds more readily to small field variations along 90°, consistent with a larger reversible rotation or domain-wall displacement contribution before irreversible switching. The larger loop area at 0° (354.8 arb. units) relative to 90° (287.5 arb. units) reflects a stronger overall hysteretic response along the preferred direction. The moderate squareness in both orientations indicates that the Kerr reversal is not ideally abrupt but includes appreciable reversible and distributed switching contributions [42], [43].

Alloying with a small amount of Al substantially modifies this balance. For NiAl-1, the easy axis rotates from 0° to 90°. The 90° Kerr loop exhibits ⟨Hc⟩ = 108.2 ± 0.5 Oe and S = 0.662 ± 0.003, whereas the 0° values are 85.5 ± 0.5 Oe and 0.476 ± 0.003. The increase in S indicates a larger remanent Kerr response along 90°, consistent with a more strongly defined preferred magnetization state. The initial susceptibility increases from 0.00144 ± 0.00005 Oe^{-1} at 0° to 0.00783 ± 0.00005 Oe^{-1} at 90°, demonstrating that the Al-modified lattice affects not only the switching field but also the low-field portion of the Kerr loop. The larger 90° loop area (389.1 arb. units vs. 207.3 arb. units at 0°) further confirms the strong orientation dependence of the field-driven Kerr response. This easy-axis rotation occurs together with a redistribution of the loop shape rather than a simple increase in Hc, suggesting that competing anisotropy contributions have changed sign or relative magnitude. Al-induced lattice distortion and deposition-induced stress can modify the magnetoelastic anisotropy, while changes in texture alter the crystallographic contribution [44].

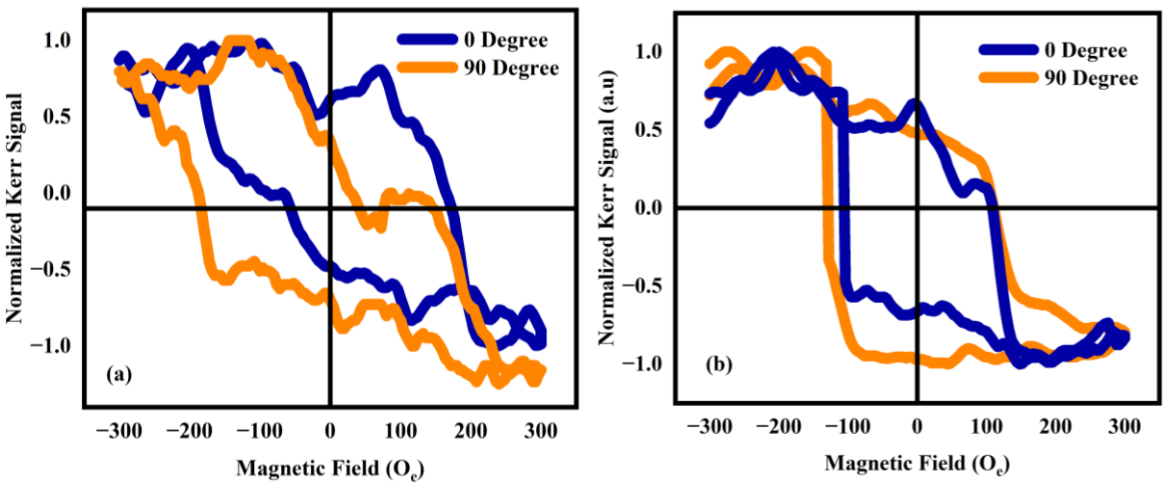

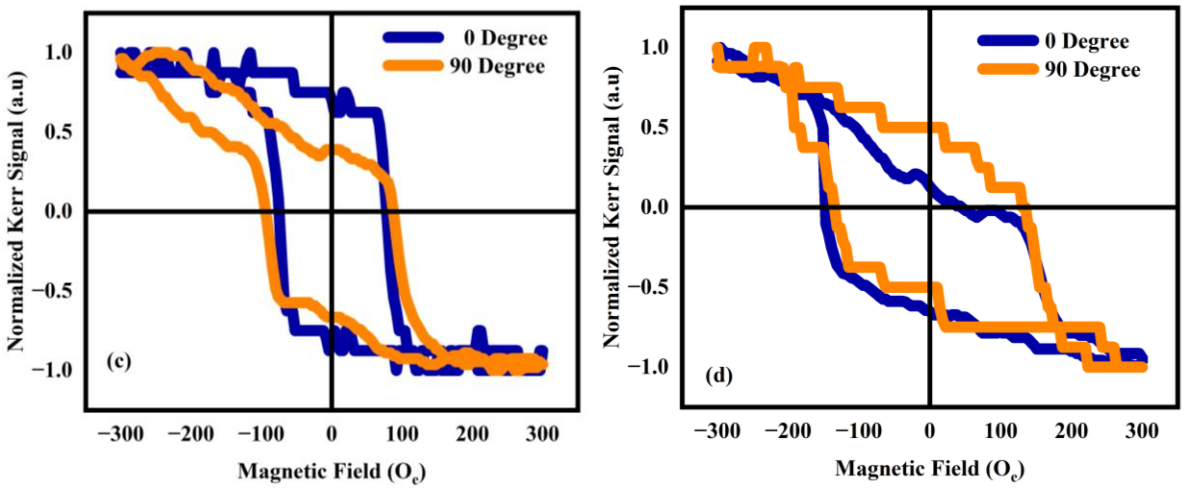

Figure 11. Longitudinal magneto-optical Kerr effect (MOKE) hysteresis loops of the Al-doped Ni thin films measured with the magnetic field applied along two orthogonal in-plane directions (0° and 90°): (a) NiAl-0, (b) NiAl-1, (c) NiAl-2, and (d) NiAl-3. All loops are normalized to the saturation Kerr signal.

The effect is most pronounced at the NiAl-2 composition. The 0° Kerr loop exhibits the lowest coercivity of the series, $\langle Hc \rangle = 80.0 \pm 0.5$ Oe, together with the highest squareness, $S = 0.708 \pm 0.003$. The initial susceptibility reaches $\chi_0 = 0.0208 \pm 0.0005$ Oe^{-1}, the highest value measured across all compositions. These parameters indicate that the Kerr signal responds strongly to small field changes near the origin, the characteristic switching field is low, and a large fraction of the saturated Kerr response remains at zero field. Thus, the magnetization component detected along 0° is both highly field responsive and strongly retained after field removal [45].

This optimized response can be associated with the balance reached at intermediate Al concentration. Substitutional Al atoms perturb the Ni lattice sufficiently to modify the local strain state and anisotropy without producing the degree of magnetic or structural disorder associated with the highest concentration. If this modification reduces dominant pinning barriers while favoring a particular in-plane texture or stress state, domain nucleation and subsequent magnetization rotation can occur at lower fields, explaining the reduction of Hc from 116.2 Oe in NiAl-0 to 80.0 Oe in NiAl-2. The improved directional ordering of the magnetization accounts for the increase in S from 0.545 to 0.708 [46].

The strong enhancement of χ_0 in NiAl-2 is particularly significant. The value increases by more than a factor of four relative to the 0° response of NiAl-0. Because χ_0 is determined from the initial slope of the Kerr-field curve, this indicates a much stronger variation of the measured longitudinal magnetization component with applied field in the low-field region. Such a response is consistent with a reduced effective barrier for field-driven magnetization rotation and/or displacement of mobile domain boundaries. The simultaneous high squareness demonstrates that this enhanced field sensitivity does

not arise from a weakly constrained magnetic state; rather, the film retains a well-defined preferred orientation after field removal [47].

The orthogonal 90° response of NiAl-2 confirms the strength of this anisotropy. The coercivity increases to 90.0 ± 0.5 Oe, while S falls sharply to 0.389 ± 0.003 and χ_0 becomes approximately 0.001 Oe^{-1}. Thus, the 0° and 90° Kerr loops possess markedly different low-field slopes and remanent responses. The 0° loop area (198.6 arb. units) is lower than the 90° value (228.4 arb. units). Although the areas are expressed in arbitrary units and represent relative hysteretic responses rather than absolute magnetic energy densities, the simultaneous occurrence of smaller area, low coercivity, high susceptibility, and high squareness along 0° establishes NiAl-2 as the most efficient reversal state in the series [48].

At higher Al concentration, the favorable balance established in NiAl-2 is disrupted. In NiAl-3, the easy direction rotates again to 90°, where ⟨Hc⟩ reaches 128.0 ± 0.5 Oe, while the 0° direction gives 91.0 ± 0.5 Oe. The corresponding S values are 0.500 ± 0.003 and 0.382 ± 0.003, respectively. Thus, the highest Al concentration produces a reversal state requiring the largest switching field while simultaneously reducing the remanent Kerr response compared with the optimum composition. This behavior suggests that the structural and magnetic modifications caused by increasing Al beyond the optimum level no longer reduce pinning but instead broaden the distribution of local switching fields [49].

Increased substitutional disorder can produce spatial variations in the local Ni environment and exchange interaction. Simultaneously, changes in lattice strain and texture can generate a wider distribution of local anisotropy energies. Variations in grain size, orientation, and defect density further modify the local domain-wall pinning landscape. The resulting magnetic film is therefore unlikely to reverse through a single dominant switching process; instead, different regions become unstable at different applied fields, producing a broadened and multi-stage Kerr response [50].

This interpretation is directly supported by the step-like features observed in the NiAl-3 MOKE loops. Unlike the relatively sharp Kerr reversal in lower-Al films, the multiple switching steps indicate that the optically sampled magnetic region contains components with different characteristic switching fields. Such behavior is particularly significant in MOKE because the probe averages the magneto-optical response over the illuminated area; consequently, multiple switching events arise when different domains or microstructural regions within that area reverse sequentially. The step-like Kerr response therefore provides direct experimental evidence for a broader switching-field distribution in NiAl-3 [51].

The extracted χ_0 and loop area are consistent with this interpretation. For NiAl-3, χ_0 is 0.0052 ± 0.0005 Oe^{-1} at 0° and decreases to 0.0021 ± 0.0005 Oe^{-1} at 90°. The relatively small low-field slope along the 90° easy direction indicates that the Kerr signal changes comparatively slowly around the origin before the major switching events occur. Once the local switching thresholds are reached, however, the

magnetization changes over a broader field range, producing the large 90° loop area of 386.5 arb. units. In contrast, the 0° loop has a smaller area of 232.7 arb. units. Thus, the large loop area at 90° reflects the extended hysteretic field range associated with the more difficult and distributed reversal process rather than stronger magnetization [52].

The complete composition dependence can therefore be understood as a competition between two effects produced by Al. At low-to-intermediate concentration, the substitutional modification of the Ni lattice favorably tunes strain, texture, local anisotropy, and magnetic coupling, reducing the effective barriers for reversal while strengthening the preferred in-plane orientation. This produces the progressive reduction in Hc and enhancement of S and χ_0 observed up to NiAl-2. Beyond this optimum concentration, increasing chemical and structural disorder becomes dominant. The resulting spatial variation in local anisotropy and pinning broadens the switching-field distribution, increases Hc, reduces squareness, and generates the multi-step Kerr reversal observed in NiAl-3 [53].

The alternating easy-axis orientation (0° → 90° → 0° → 90° for NiAl-0 through NiAl-3) provides further evidence that the effective anisotropy is governed by competing contributions rather than a single intrinsic term. In the present films, Al-induced changes in crystallographic texture and residual stress are particularly important because they modify the magnetoelastic contribution to the in-plane anisotropy. The magneto-crystalline contribution is simultaneously affected by changes in the local crystal environment and texture, while microstructural changes influence domain-wall pinning and local switching fields. The easy direction observed by MOKE therefore corresponds to the orientation at which the combined anisotropy landscape permits the most favorable reversal and remanent magnetization response under the measurement conditions [54].

The trends in the four MOKE-derived parameters reinforce this interpretation. The easy-axis Hc decreases from 116.2 Oe for NiAl-0 to 108.2 Oe for NiAl-1 and reaches 80.0 Oe for NiAl-2, before increasing sharply to 128.0 Oe for NiAl-3. Over the same sequence, the easy-axis S evolves from 0.545 to 0.662 to 0.708 before decreasing to 0.500. The initial susceptibility likewise reaches its maximum at NiAl-2, while the loop shape changes from relatively smooth reversal in the lower-Al films to distinctly multi-step switching in NiAl-3. The simultaneous optimization of these independent characteristics at NiAl-2 strongly indicates that this composition represents a transition point between reduced pinning and increased disorder [55].

Therefore, the MOKE results demonstrate that Al does not merely alter the magnitude of the magnetic response; it restructures the entire field-dependent reversal pathway of the Ni film. Moderate Al-induced lattice and microstructural modification produce a well-defined anisotropic state with low switching field, high remanent Kerr response, and strong low-field susceptibility. Excessive Al, in contrast, introduces sufficient local structural and magnetic variation to broaden the switching-field distribution and promote sequential reversal of different magnetic regions. Consequently, NiAl-2 exhibits the most

favorable MOKE characteristics, with the lowest easy-axis ⟨Hc⟩ (80.0 ± 0.5 Oe), highest S (0.708 ± 0.003), highest χ_0 (0.0208 ± 0.0005 Oe^{-1}), and lowest easy-axis loop area (198.6 arb. units), whereas NiAl-3 displays the most complex and field-demanding reversal behavior [56].

Table 6. Magnetic parameters Coercivity (⟨Hc⟩), squareness (S = Mr/Ms), initial susceptibility (χ_0), and loop area extracted from the longitudinal MOKE hysteresis loops of the Al-doped Ni thin films (NiAl-0 to NiAl-3) measured along the 0° and 90° in-plane directions.

Sample	Angle	$\langle H_c \rangle$ (Oe)	S	χ_0 (Oe^{-1})	Loop Area (arb. units)
NiAl-0	0° (easy)	116.2 ± 0.5	0.545 ± 0.003	0.00464 ± 0.00005	354.8
	90°	109.0 ± 0.5	0.521 ± 0.003	0.01238 ± 0.00005	287.5
NiAl-1	0°	85.5 ± 0.5	0.476 ± 0.003	0.00144 ± 0.00005	207.3
	90° (easy)	108.2 ± 0.5	0.662 ± 0.003	0.00783 ± 0.00005	389.1
NiAl-2	0° (easy)	80.0 ± 0.5	0.708 ± 0.003	0.0208 ± 0.0005	198.6
	90°	90.0 ± 0.5	0.389 ± 0.003	~0.001*	228.4
NiAl-3	0°	91.0 ± 0.5	0.382 ± 0.003	0.0052 ± 0.0005	232.7
	90° (easy)	128.0 ± 0.5	0.500 ± 0.003	0.0021 ± 0.0005	386.5

** Approximate value.*

The magnetic behavior of Al-doped Ni thin films is governed by a distinct structure–property hierarchy spanning crystallite refinement, crystallographic mosaicity, and surface morphology. Coercivity evolution deviates from classical grain-size scaling, exhibiting a nonmonotonic response consistent with competing pinning mechanisms, while mosaic spread exerts a stronger influence on switching-field distribution than crystallite size alone. Surface roughness inversely correlates with initial susceptibility, indicating that morphological disorder introduces heterogeneous nucleation barriers that degrade low-field magnetic response. The correlation between coercivity and crystallite size reveals a departure from the expected grain-boundary pinning regime. The NiAl-2 film, with a crystallite size of approximately 12 nm, exhibits the lowest coercivity, whereas the smaller-crystallite NiAl-3 sample (8.7 nm) shows the highest coercivity. This reversal implies that at high Al concentrations, lattice strain and dislocation density dominate the pinning landscape, overriding the simple inverse relationship between grain size and coercivity. This behavior is consistent with findings in Ni-Al systems where excess Al content induces supersaturation and lattice distortion that strengthen pinning beyond the contribution of grain refinement [57], [58].

Mosaic spread, measured by the full width at half maximum of the ω-scan rocking curve, provides a more direct correlation with coercivity than crystallite size. The progressive increase in mosaicity from 13.94° to 20.29° reflects a broadening angular distribution of crystallite orientations, which translates directly into a wider spread of local magnetic easy axes. This broadening produces a multi-step reversal process in the NiAl-3 film, as evidenced by the step-like features in the MOKE loops, confirming that crystallographic misorientation governs the switching-field distribution rather than grain size alone. The mosaic spread therefore acts as a structural proxy for the effective anisotropy field distribution in these polycrystalline films. Surface roughness exhibits an inverse correlation with initial susceptibility,

linking morphological disorder to low-field magnetic response. The smoothest film (NiAl-2, Ra ≈ 4 nm) displays the highest initial susceptibility, while the rougher films exhibit systematically lower values. Rougher surfaces introduce heterogeneous nucleation sites and local demagnetizing fields that impede reversible domain-wall motion at low applied fields, thereby reducing susceptibility. This relationship is consistent with molecular dynamics simulations demonstrating that increased incident energy during deposition roughens the surface and increases vacancy content, both of which degrade low-field magnetic response. This concentration-dependent evolution establishes a clear optimum in the Al-modified Ni system and demonstrates that the magnetic anisotropy and reversal dynamics can be effectively tuned through controlled modification of the alloy composition [59].

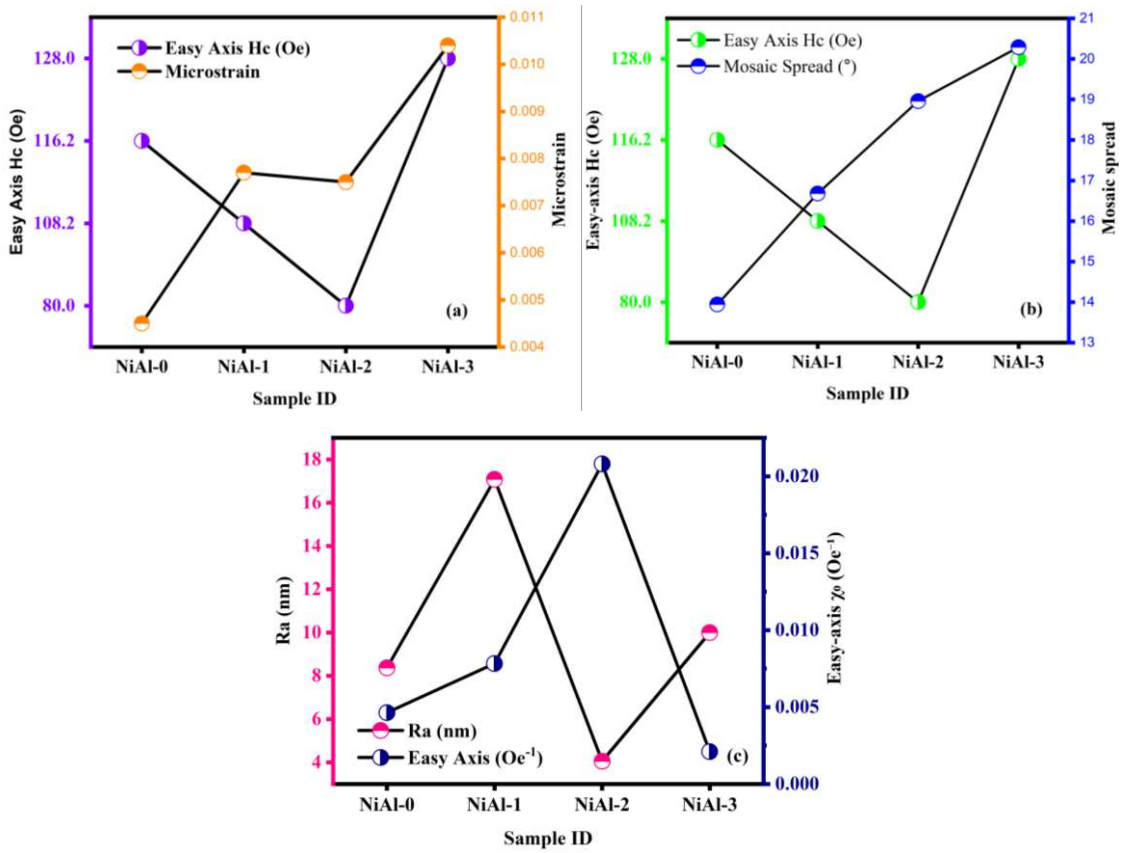

Figure 12. Structure-property correlations in Al-doped Ni thin films: (a) easy-axis coercivity and microstrain, (b) easy-axis coercivity and mosaic spread, and (c) surface roughness and easy-axis initial susceptibility, all plotted against Al content (NiAl-0 to NiAl-3).

Conclusion

This study systematically establishes the correlation between Al-induced crystallographic and microstructural evolution and the magnetic anisotropy and magnetization reversal of magnetron-sputtered polycrystalline Ni-Al thin films containing 0, 3, 5, and 8 wt.% Al. HRXRD and GIXRD analyses confirm a progressive shift of the Ni (111) reflection toward higher diffraction angles, accompanied by a reduction in d-spacing from 0.20457 to 0.20266 nm and crystallite size from 20.17

to 8.71 nm. Concurrent increases in microstrain from 0.0045 to 0.0104 and dislocation density from 2.46×10^{-3} to 1.32×10^{-2} nm^{-2}, together with increased rocking-curve width and reduced in-plane texture, demonstrate progressive structural disorder with Al incorporation. XRR reveals a monotonic decrease in film density from 8.75 to 7.78 g cm^{-3}, consistent with the substitution of higher-density Ni by lower-density Al, while the substrate roughness initially decreases and then increases at the highest Al content. FESEM confirms a progressive refinement of the nanogranular surface morphology, and AFM shows that the average surface roughness reaches its minimum at the intermediate composition, consistent with the most uniform grain population.

Longitudinal MOKE measurements demonstrate that these structural modifications strongly affect the in-plane magnetic anisotropy and reversal pathway. The undoped Ni film exhibits a preferred 0° direction and an approximately 48 Oe loop displacement, whereas Al incorporation produces a non-monotonic evolution of the preferred magnetic direction. The 5 wt.% Al film exhibits the most favorable reversal characteristics, with an easy-axis coercivity of 80.0 ± 0.5 Oe, squareness of 0.708 ± 0.003, and initial susceptibility of 0.0208 ± 0.0005 Oe^{-1}. Further Al incorporation increases the easy-axis coercivity to 128.0 ± 0.5 Oe and promotes pronounced multistep reversal, indicating a broader switching-field distribution associated with increased defect density, grain-boundary population, and local anisotropy fluctuations.

The structure–property correlations extracted from the combined XRD, XRR, AFM, and MOKE data reveal three key relationships. First, coercivity deviates from classical grain-size scaling: the film with the smallest crystallite size (NiAl-3, 8.7 nm) exhibits the highest coercivity, while the intermediate composition (NiAl-2, 12 nm) exhibits the lowest, indicating that lattice strain and dislocation density dominate the pinning landscape at high Al content. Second, mosaic spread provides a more direct correlation with coercivity than crystallite size, confirming that the angular distribution of crystallite orientations controls the switching-field distribution and the onset of multistep reversal. Third, surface roughness is inversely correlated with initial susceptibility, indicating that morphological disorder introduces heterogeneous nucleation barriers that degrade the low-field magnetic response. Together, these correlations demonstrate that the magnetic behavior of Al-doped Ni thin films is governed by a hierarchy of structural features spanning crystallite refinement, crystallographic mosaicity, and surface morphology. The established structure–magnetism correlation provides a quantitative basis for engineering Ni-based magnetic thin films with controlled magnetization reversal for spintronic and magnetic sensing applications.

CRediT authorship contribution statement

Qurat ul Ain: Fabrication & Characterization, Writing-original draft, visualization, conceptualization
Ali Tahir: Supervision, Writing-original draft, Review & editing**,** software, visualization & validation

Anam Ayub Tahami: Formal analysis, Data curation, Conceptualization, **Arzoo Fatima**: Methodology, Investigation,

Declaration of competing interest: The authors declare that they have no known competing financial interests or personal relationships that could have appeared to influence the work reported in this paper.

Data availability: Data will be made available on request from the corresponding author.

References

[1] N. Kaplan, H. Kuru, and H. Köçkar, "Investigation of the influence of Al layer and total film thicknesses on structural and related magnetic properties in sputtered Ni/Al multilayer thin films," *Journal of Materials Science: Materials in Electronics*, vol. 35, no. 4, p. 302, Feb. 2024, doi: 10.1007/s10854-024-12008-6.

[2] A. Sharma, S. Mohan, and S. Suwas, "The effect of the deposition rate on the crystallographic texture, microstructure evolution and magnetic properties in sputter deposited Ni-Mn-Ga thin films," *Thin Solid Films*, vol. 616, pp. 530–542, Oct. 2016, doi: 10.1016/j.tsf.2016.08.033.

[3] C. Nacereddine *et al.*, "Structural, electrical and magnetic properties of evaporated Ni/Cu and Ni/glass thin films," *Materials Science and Engineering: B*, vol. 136, no. 2–3, pp. 197–202, Jan. 2007, doi: 10.1016/j.mseb.2006.09.021.

[4] N. D. Suliţanu, "Electrochemical deposition of novel nanostructured magnetic thin films for advanced applications," *Materials Science and Engineering: B*, vol. 95, no. 3, pp. 230–235, Sep. 2002, doi: 10.1016/S0921-5107(02)00237-4.

[5] K. Hedayati and G. Nabiyouni, "Surface roughness analysis and magnetic property studies of nickel thin films electrodeposited onto rotating disc electrodes," *Applied Physics A*, vol. 116, no. 4, pp. 1605–1612, Sep. 2014, doi: 10.1007/s00339-014-8288-4.

[6] W. Ahmad *et al.*, "Strain tuned magnetic anisotropy in nickel–zinc ferrite thin films," *Journal of Physics: Condensed Matter*, vol. 37, no. 42, p. 425801, Oct. 2025, doi: 10.1088/1361-648X/ae0f32.

[7] C. Zhou, L. Yan, B. Yan, and Z. Han, "Structure and Magnetic Properties of Iron Thin Films Prepared at Different Deposition Times," *Materials*, vol. 19, no. 1, p. 165, Jan. 2026, doi: 10.3390/ma19010165.

[8] A. Khapikov, L. Uspenskaya, J. Ebothe, and S. Vilain, "Change of the magnetization reversal mechanism of polycrystalline Ni-Co thin films," *Phys. Rev. B*, vol. 57, no. 23, pp. 14990–14998, Jun. 1998, doi: 10.1103/PhysRevB.57.14990.

[9] S. Guan *et al.*, "Microstrain and its effect on magnetization reversal in sintered Nd-Fe-B magnets," *Acta Mater.*, vol. 319, p. 122688, Oct. 2026, doi: 10.1016/j.actamat.2026.122688.

[10] A. B. Drovosekov *et al.*, "Magnetic anisotropy of polycrystalline high-temperature ferromagnetic Mn x Si 1-x (<math altimg="si0021.gif" overflow="scroll"> <mrow> <mi>x</mi> <mo>≈</mo> <mn>0.5</mn> </mrow> </math>) alloy films," *J. Magn. Magn. Mater.*, vol. 429, pp. 305–313, May 2017, doi: 10.1016/j.jmmm.2017.01.022.

[11] P. Stefanov and A. Stanchev, “Surface segregation and preferential sputtering in thin Al–Ni alloy films,” *Mater. Chem. Phys.*, vol. 50, no. 3, pp. 209–212, Oct. 1997, doi: 10.1016/S0254-0584(97)01935-4.

[12] A. Khapikov, L. Uspenskaya, J. Ebothe, and S. Vilain, “Change of the magnetization reversal mechanism of polycrystalline Ni-Co thin films,” *Phys. Rev. B*, vol. 57, no. 23, pp. 14990–14998, Jun. 1998, doi: 10.1103/PhysRevB.57.14990.

[13] I. V. Soldatov, J. Zehner, K. Leistner, T. Kang, D. Karnaushenko, and R. Schäfer, “Advanced, Kerr-microscopy-based MOKE magnetometry for the anisotropy characterisation of magnetic films,” *J. Magn. Magn. Mater.*, vol. 529, p. 167889, Jul. 2021, doi: 10.1016/j.jmmm.2021.167889.

[14] K. Légaré *et al.*, “Analytic description and optimization of magneto-optical Kerr setups with photoelastic modulation,” *Review of Scientific Instruments*, vol. 93, no. 7, Jul. 2022, doi: 10.1063/5.0088610.

[15] A. Das and D. Bhattacharya, “Effect of post-deposition annealing and substrate heating on structural and magnetic properties of nano-structured sputtered nickel thin films,” *Bulletin of Materials Science*, vol. 49, no. 1, p. 40, Feb. 2026, doi: 10.1007/s12034-026-03563-1.

[16] K. A. B. Andersson, H. T. G. Nilsson, and S.-E. Karlsson, “Composition-dependent structural and morphological changes in nickel-aluminium films prepared by co- evaporation of the pure metals,” *Thin Solid Films*, vol. 58, no. 2, pp. 345–351, Apr. 1979, doi: 10.1016/0040-6090(79)90269-4.

[17] Z. Chen *et al.*, “Formation of coherent nanocomposite structure in nickel-aluminum alloys synthesized far from equilibrium,” *Acta Mater.*, vol. 302, p. 121674, Jan. 2026, doi: 10.1016/j.actamat.2025.121674.

[18] F. J. Santos López *et al.*, “Study of magnetic and structural properties of nickel films deposited by magnetron sputtering using a powder target,” *Physica B Condens. Matter*, vol. 725, p. 418172, Mar. 2026, doi: 10.1016/j.physb.2025.418172.

[19] N. Kaplan, H. Kuru, and H. Köçkar, “Investigation of the influence of Al layer and total film thicknesses on structural and related magnetic properties in sputtered Ni/Al multilayer thin films,” *Journal of Materials Science: Materials in Electronics*, vol. 35, no. 4, p. 302, Feb. 2024, doi: 10.1007/s10854-024-12008-6.

[20] N. Toncich, F. Schwarz, R. A. Gallivan, J. Gillon, and R. Spolenak, “Composition Effects on Ni/Al Reactive Multilayers: A Comprehensive Study of Mechanical Properties, Reaction Dynamics and Phase Evolution,” Feb. 2025, doi: 10.1063/5.0263283.

[21] F. Geenen, K. van Stiphout, J. L. Jordan-Sweet, A. Vantomme, C. Lavoie, and C. Detavernier, “The influence of Al alloying on silicide formation, morphology and texture between a thin (<20 nm) Ni film and Si(001),” 2015. [Online]. Available: https://api.semanticscholar.org/CorpusID:138812023

[22] M. Nur, E. Alam, and A. Nasim, “Magnetron sputtering of nanolaminates with materials designed and engineered properties,” 2020.

[23] J. Xie, T. Lin, and C. Wang, “Molecular dynamics study of the effects of deposition parameters on Si0.5Ge0.5 film growth on Ge(100) substrate,” *Comput. Mater. Sci.*, vol. 256, p. 113981, Jun. 2025, doi: 10.1016/j.commatsci.2025.113981.

[24] A. I. Dmitriev, A. Yu. Nikonov, and W. Österle, “Molecular dynamics sliding simulations of amorphous Ni, Ni-P and nanocrystalline Ni films,” *Comput. Mater. Sci.*, vol. 129, pp. 231–238, Mar. 2017, doi: 10.1016/j.commatsci.2016.12.039.

[25] I. Sankowska, A. Jasik, and K. Piskorski, “Structural and optical characterization of type I AlSb/GaSb superlattices by means of high-resolution X-ray diffraction, X-ray reflectivity and Raman spectroscopy,” *Appl. Surf. Sci.*, vol. 710, p. 163921, Nov. 2025, doi: 10.1016/j.apsusc.2025.163921.

[26] H. Verma, K. Le Guen, S. Gupta, R. Dhawan, M. H. Modi, and P. Jonnard, “Interface analysis of Mg/Sc and Sc/Mg bilayers using X-ray reflectivity,” *Thin Solid Films*, vol. 763, p. 139595, Dec. 2022, doi: 10.1016/j.tsf.2022.139595.

[27] M. Dolores Merchán *et al.*, “Structure of graphene oxide-phospholipid monolayers: A grazing incidence X-ray diffraction and neutron and X-ray reflectivity study,” *J. Colloid Interface Sci.*, vol. 655, pp. 664–675, Feb. 2024, doi: 10.1016/j.jcis.2023.11.022.

[28] K. T. Kim *et al.*, “X-ray reflectivity data analysis using Bayesian inference: The study of induced Pt magnetization in Pt/Co/Pt,” *Current Applied Physics*, vol. 30, pp. 46–52, Oct. 2021, doi: 10.1016/j.cap.2021.04.025.

[29] Kiranjot, R. Dhawan, R. K. Gupta, P. K. Yadav, and M. H. Modi, “Interface asymmetry in AlN/Ni and Ni/AlN interfaces: A study using resonant soft X-ray reflectivity,” *Appl. Surf. Sci.*, vol. 529, p. 147199, Nov. 2020, doi: 10.1016/j.apsusc.2020.147199.

[30] L. Zhang, C. Xie, and J. Wu, “Grain size estimations of annealed Ti–Ni shape memory thin films,” *J. Alloys Compd.*, vol. 432, no. 1–2, pp. 318–322, Apr. 2007, doi: 10.1016/j.jallcom.2006.06.018.

[31] M. J. Morán, A. M. Condó, and N. Haberkorn, “Recrystallization and martensitic transformation in nanometric grain size Cu-Al-Ni thin films grown by DC sputtering at room temperature,” *Mater. Charact.*, vol. 139, pp. 446–451, May 2018, doi: 10.1016/j.matchar.2018.03.025.

[32] J. M. Gómez-Guzmán and S. Pütter, “Stress minimization in DC-sputtered nickel thin films for optimized high-m-value Ni/Ti neutron supermirrors,” *Nucl. Instrum. Methods Phys. Res. A*, vol. 1093, p. 172078, Jan. 2027, doi: 10.1016/j.nima.2026.172078.

[33] Y. Yang, K. Ding, T. Zhu, J. Kacher, and O. Pierron, “The role of grain size distribution on the anomalous yielding of ultrafine-grained Au thin films,” *Scr. Mater.*, vol. 275, p. 117178, Apr. 2026, doi: 10.1016/j.scriptamat.2026.117178.

[34] M. N. Baig, W. Ahmed, F. A. Khalid, R. M. Said, and J. McLaughlin, “Properties of NiAl and Ni-Al-N Thin Films Deposited by Closed Field Unbalanced Magnetron Sputter Ion Plating Using Elemental Ni and Al Targets,” *J. Nanosci. Nanotechnol.*, vol. 9, no. 7, pp. 4034–4039, Jul. 2009, doi: 10.1166/jnn.2009.M07.

[35] J. P. Liu *et al.*, “X-ray reflectivity measurement of interdiffusion in metallic multilayers during rapid heating,” *J. Synchrotron Radiat.*, vol. 24, no. 4, pp. 796–801, Jul. 2017, doi: 10.1107/S1600577517008013.

[36] T.-C. Hung *et al.*, “Promoted activity of annealed Rh nanoclusters on thin films of Al_2O_3 /NiAl(100) in the dehydrogenation of Methanol-d_4,” *RSC Adv.*, vol. 11, no. 40, pp. 24762–24771, 2021, doi: 10.1039/D1RA04066A.

[37] C. T. Wang, C. W. Lin, C. L. Hsia, B. W. Chang, and M. F. Luo, “Under-surface observation of thin-film alumina on NiAl(100) with scanning tunneling microscopy,” *Thin Solid Films*, vol. 520, no. 11, pp. 3952–3959, Mar. 2012, doi: 10.1016/j.tsf.2012.01.011.

[38] İ. Kanmaz, T. Bayazit, F. Güngör, and M. Tomakin, “Comparative analysis of Al and Ni dopants on the optical, structural and electrical properties of CeO2 thin films,” *Opt. Mater. (Amst).*, vol. 175, p. 118057, Jul. 2026, doi: 10.1016/j.optmat.2026.118057.

[39] K. Kandhasamy *et al.*, “Controlled surface nanostructuring and functional property enhancement in Se–Te–Sn–Ag thin films by 100 MeV Ni^{8+} ion irradiation,” *Surfaces and Interfaces*, vol. 98, p. 110289, Oct. 2026, doi: 10.1016/j.surfin.2026.110289.

[40] E. Heidari, S. Moazami, A. Bahrami, and S. Torkian, “On the microstructure, electrochemical properties, biocompatibility, and cytotoxicity of TiAlFeCoX (X=Ni, Cu) high-entropy alloy thin films, deposited by DC magnetron sputtering,” *Mater. Chem. Phys.*, vol. 337, p. 130617, Jun. 2025, doi: 10.1016/j.matchemphys.2025.130617.

[41] N. Shukla, M. Gupta, Z. Hussain, V. R. Reddy, and S. Chaudhary, “Substrate-morphology-induced magnetic anisotropy and magnetization reversal in epitaxial Fe4N thin films,” *J. Alloys Compd.*, vol. 1044, p. 184275, Nov. 2025, doi: 10.1016/j.jallcom.2025.184275.

[42] A. Lo Giudice, A. Roman, and L. B. Steren, “Magnetization reversal and anisotropies in buffered transition-metal alloys thin films,” *J. Magn. Magn. Mater.*, vol. 642, p. 173868, Mar. 2026, doi: 10.1016/j.jmmm.2026.173868.

[43] N. Mondal, A. Barman, S. Chatterjee, and D. Mukherjee, “Influence of twin-crystal structures on the temperature dependence of magneto-optic Kerr effect and magnetic anisotropy in epitaxial Ni thin films,” *J. Magn. Magn. Mater.*, vol. 564, p. 170118, Dec. 2022, doi: 10.1016/j.jmmm.2022.170118.

[44] M. Del Canto, V. Solís Lazo, D. Alburquenque, E. Saavedra, and J. Escrig, “Magnetization reversal in nickel nanoparticle assemblies revealed by experiment and image-based micromagnetic simulations,” *Physica B Condens. Matter*, vol. 744, p. 419473, Jan. 2027, doi: 10.1016/j.physb.2026.419473.

[45] S. Bai *et al.*, “Effect of Er and Al co-doping on the microstructures, magnetic properties, and magnetization reversal of sintered (Nd,Pr)–Fe–B magnets,” *J. Magn. Magn. Mater.*, vol. 655, p. 174279, Oct. 2026, doi: 10.1016/j.jmmm.2026.174279.

[46] A. S. E. Cruz, N. Nateghi, F. Béron, C. Lacroix, and D. Ménard, “Isothermal remanent magnetization measurements of oriented MnP nanoparticles embedded in a GaP epilayer,” *J. Magn. Magn. Mater.*, vol. 656, p. 174517, Oct. 2026, doi: 10.1016/j.jmmm.2026.174517.

[47] J. Yoon, C.-Y. You, and M.-H. Jung, “Dynamic susceptibility of thin films with perpendicular magnetic anisotropy,” *Current Applied Physics*, vol. 13, no. 8, pp. 1765–1768, Oct. 2013, doi: 10.1016/j.cap.2013.07.011.

[48] A. P. Kotti and A. C. Mishra, “Angular magnetization reversal of thin permalloy conical nanotubes with circumferential anisotropy,” *Physica B Condens. Matter*, vol. 723, p. 418114, Feb. 2026, doi: 10.1016/j.physb.2025.418114.

[49] L. F. S. Azeredo, H. S. Acosta, A. M. H. de Andrade, and J. Geshev, “Inducing and/or redirecting magnetic anisotropy in Co films with collapsed hard-magnetization axes,” *J. Magn. Magn. Mater.*, vol. 640, p. 173805, Feb. 2026, doi: 10.1016/j.jmmm.2025.173805.

[50] C. Das, P. Alagarsamy, and S. Bedanta, “Dynamics of magnetization reversal and enhanced magnetic properties in FeTaC/SiO2 multilayer thin films,” *J. Magn. Magn. Mater.*, vol. 634, p. 173590, Nov. 2025, doi: 10.1016/j.jmmm.2025.173590.

[51] S. A. Elmakki, A. Boubekri, L. Mouakkir, A. Farchakh, and M. El Hafidi, “Magnetization, susceptibility and reentrant behavior in a ferrimagnetic bilayer Kagome structure,” *J. Magn. Magn. Mater.*, vol. 656, p. 174474, Oct. 2026, doi: 10.1016/j.jmmm.2026.174474.

[52] M. Del Canto, V. Solís Lazo, D. Alburquenque, E. Saavedra, and J. Escrig, “Magnetization reversal in nickel nanoparticle assemblies revealed by experiment and image-based micromagnetic simulations,” *Physica B Condens. Matter*, vol. 744, p. 419473, Jan. 2027, doi: 10.1016/j.physb.2026.419473.

[53] K. He *et al.*, “Magnetic field direction dependent magnetization reversal in synthetic antiferromagnets based on first-order reversal curve analysis,” *J. Magn. Magn. Mater.*, vol. 614, p. 172728, Feb. 2025, doi: 10.1016/j.jmmm.2024.172728.

[54] A. S. Komlev, S. I. Kostylev, A. V. Finko, N. N. Perova, T. Y. Kiseleva, and N. S. Perov, “In-situ magnetization relaxation during the crystallization in amorphous magnetic ribbons,” *J. Alloys Compd.*, vol. 1064, p. 187860, Apr. 2026, doi: 10.1016/j.jallcom.2026.187860.

[55] S. K. Mishra *et al.*, “Phase-transition induced magnetic domain evolution and magnetization dynamics in FePt/FeRh Bilayers for advanced heat-assisted magnetic recording,” *J. Alloys Compd.*, vol. 1079, p. 189801, Aug. 2026, doi: 10.1016/j.jallcom.2026.189801.

[56] A. S. Komlev, S. I. Kostylev, A. V. Finko, N. N. Perova, T. Y. Kiseleva, and N. S. Perov, “In-situ magnetization relaxation during the crystallization in amorphous magnetic ribbons,” *J. Alloys Compd.*, vol. 1064, p. 187860, Apr. 2026, doi: 10.1016/j.jallcom.2026.187860.

[57] D. Li *et al.*, “Spin-orbit torque induced field-free magnetization switching in rare-earth Pt/[Sm/Co]3 magnetic multilayers with a vertical composition gradient,” *J. Alloys Compd.*, vol. 1064, p. 187987, Apr. 2026, doi: 10.1016/j.jallcom.2026.187987.

[58] S. A. Elmakki, A. Boubekri, L. Mouakkir, A. Farchakh, and M. El Hafidi, “Magnetization, susceptibility and reentrant behavior in a ferrimagnetic bilayer Kagome structure,” *J. Magn. Magn. Mater.*, vol. 656, p. 174474, Oct. 2026, doi: 10.1016/j.jmmm.2026.174474.

[59] C. Das, P. Alagarsamy, and S. Bedanta, “Dynamics of magnetization reversal and enhanced magnetic properties in FeTaC/SiO2 multilayer thin films,” *J. Magn. Magn. Mater.*, vol. 634, p. 173590, Nov. 2025, doi: 10.1016/j.jmmm.2025.173590.